J. Fluid Mech. (1994), *vol.* 265, *pp.* 25–64

Three-dimensionalization of barotropic vortices on the *f*-plane

By W. D. SMYTH[1] AND W. R. PELTIER[2]

[1] College of Oceanography and Atmospheric Sciences, Oregon State University, Corvallis OR 97331, USA

[2] Department of Physics, University of Toronto, Toronto, Ontario M5S 1A7, Canada

(Received 29 October 1992 and in revised form 21 September 1993)

We examine the stability characteristics of a two-dimensional flow which consists initially of an inflexionally unstable shear layer on an *f*-plane. Under the action of the primary instability, the vorticity in the shear-layer initially coalesces into two Kelvin–Helmholtz vortices which subsequently merge to form a single coherent vortex. At a sequence of times during this process, we test the stability of the two-dimensional flow to fully three-dimensional perturbations. A somewhat novel approach is developed which removes inconsistencies in the secondary stability analyses which might otherwise arise owing to the time-dependence of the two-dimensional flow.

In the non-rotating case, and before the onset of pairing, we obtain a spectrum of unstable longitudinal modes which is similar to that obtained previously by Pierrehumbert & Widnall (1982) for the Stuart vortex, and by Klaassen & Peltier (1985, 1989, 1991) for more realistic flows. In addition, we demonstrate the existence of a new sequence of three-dimensional subharmonic (and therefore 'helical') instabilities. After pairing is complete, the secondary instability spectrum is essentially unaltered except for a doubling of length- and timescales that is consistent with the notion of spatial and temporal self-similarity. Once pairing begins, the spectrum quickly becomes dominated by the unstable modes of the emerging subharmonic Kelvin–Helmholtz vortex, and is therefore similar to that which is characteristic of the post-pairing regime. Also in the context of non-rotating flow, we demonstrate that the direct transfer of energy into the dissipative subrange via secondary instability is possible only if the background flow is stationary, since even slow time-dependence acts to decorrelate small-scale modes and thereby to impose a short-wave cutoff on the spectrum.

The stability of the merged vortex state is assessed for various values of the planetary vorticity *f*. Slow rotation may either stabilize or destabilize the columnar vortices, depending upon the sign of *f*, while fast rotation of either sign tends to be stabilizing. When *f* has opposite sign to the relative vorticity of the two-dimensional basic state, the flow becomes unstable to a new mode of instability that has not been previously identified. Modes whose energy is concentrated in the vortex cores are shown to be associated, even at non-zero *f*, with Pierrehumbert's (1986) elliptical instability. Through detailed consideration of the vortex interaction mechanisms which drive instability, we are able to provide physical explanations for many aspects of the three-dimensionalization process.

1. Introduction

Geophysical flows are often dominated by horizontal motions (e.g. McWilliams 1983), and insight into the dynamics of such flows may therefore often be gained

through the analysis of numerically evolved two-dimensional model flows. Such analyses have most often focused upon isotropic two-dimensional turbulence which is forced at some non-zero wavenumber (e.g. Benzi, Patarnello & Santangelo 1988). However, geophysical flows also tend to be characterized by large-scale shears in the horizontal velocity, and the resulting anisotropic effects can play a dominant role in governing their dynamical evolution (e.g. Shepherd 1987; Lesieur *et al.* 1988; Smyth 1992; Smyth & Peltier 1993). If the planetary vorticity gradient β is sufficiently small, the dynamic instability of the large-scale shear creates small vortices and subsequently induces these vortices to merge, the ultimate result being a single, long-lived coherent vortex. (We assume that the large-scale flow is zonal, and that the total flow is therefore periodic in the streamwise coordinate.) This process represents a distinct mechanism for coherent vortex generation which is considerably more efficient than the upscale energy cascade which is observed in isotropic three-dimensional turbulence experiments (Smyth & Peltier 1993), and has been suggested as a possible mechanism for the formation of large, stable vortices in the atmospheres of the giant planets (e.g. Marcus 1990).

Independently of the geophysical perspective, vortex formation in a sheared environment may be considered as one of the elemental processes that drive the downscale energy cascade in a generic turbulent flow. In this sense, the evolution of a free shear layer is a process which occupies a position of fundamental importance in fluid dynamics. Over the last few decades, an idealized picture has emerged which describes the two-dimensional evolution of temporally-growing homogeneous shear layers. (Spatially-growing shear layers evolve in a somewhat different fashion, but the essential processes are similar.) Initially, the layer rolls up into a train of discrete Kelvin–Helmholtz (KH) vortices whose wavelength is roughly seven times the initial depth of the layer. At this point, subharmonic KH instability induces adjacent vortices to begin to orbit one another and subsequently merge. The number of vortices is thereby reduced by a factor of two, while their scale is increased by a similar factor. As a result, the effective depth of the shear layer is doubled, and the advective timescale (i.e. the inverse of the overall mean shear), upon which the two-dimensional features evolve, is also doubled. This process then repeats, and because of the increase in the advection time, each subsequent merging requires about twice as long to complete as did its predecessor. As a result of the aforementioned spatial and temporal self-similarity, the depth of the shear layer grows linearly with time (e.g. Lesieur *et al.* 1988; Smyth & Peltier 1993), and encompasses progressively fewer and larger vortices.

The major caveat to general acceptance of the above described heuristic picture of free shear-layer evolution is, of course, that real flows are never perfectly two-dimensional. It is therefore essential that we assess the significance of whatever three-dimensional circulations may develop during and after the formation of large-scale vortices. Laboratory experiments with spatially growing shear layers (e.g. Wygnanski *et al.* 1979; Browand & Ho 1983) have revealed that three-dimensional motions invariably occur, but that the flow tends to remain roughly two-dimensional on the scale of the large vortices. Pierrehumbert & Widnall (1982, hereinafter PW) investigated the onset of three-dimensional motions via stability analyses of the Stuart vortex, an exact stationary solution of the Euler equations which resembles the KH vortices that occur in both numerical simulations and laboratory experiments. They found the secondary instability spectrum to consist of transverse subharmonic instabilities which lead to vortex merging, helical pairing modes which induce the vortex cores to deform into a diamond lattice when viewed from above, and the translative instability, which leads to alternating elevations and depressions of the vortex cores. Translative

instability, in particular, was found over a broad range of spanwise wavenumbers, and was therefore identified in PW as a mechanism capable of injecting energy directly into the dissipation scales. Pierrehumbert (1986; see also Bayly 1986) later associated the translative modes with a non-scale-selective instability (the *elliptical* instability) which affects any vortex provided that it exhibits non-zero ellipticity. The physical mechanism which drives the elliptical instability will be discussed in the present paper. Metcalfe *et al.* (1987) performed fully-three-dimensional numerical simulations of merging KH vortices, and found that three-dimensional motions consisted primarily of streamwise 'ribs' of vorticity which developed in the strained region between the large vortices. These structures were identified with the 'mushroom-shaped' streamwise vortices whose existence had previously been documented in the laboratory experiments of Briedenthal (1981), Bernal & Roshko (1986), Lasheras, Cho & Maxworthy (1986) and Lasheras & Choi (1988). It was suggested at that time that the translative instability could account for the emergence of these circulations. In addition, the three-dimensional simulations of Comte, Lesieur & Lamballais (1992) have revealed evidence of the helical pairing mode. Klaassen & Peltier (1991, hereinafter KP) performed stability analyses similar to those of PW, with enhanced spatial resolution and using numerically evolved KH vortices as background flows as well as Stuart vortices. In that study, the stability characteristics pertaining to the case of unstratified flow were found to be dominated by a class of modes which were referred to as the 'principal spectrum', and which were identified as the source of the streamwise vortices observed in the simulations of Metcalfe *et al.* and in the laboratory experiments of Briedenthal, Bernal & Roshko, Lasheras *et al.* and Lasheras & Choi. In this paper, we will show that the translative mode of PW is in fact a part of the principal spectrum of KP.

The time-dependence of the three-dimensionalization process is clearly of central importance. Corcos & Lin (1984), using a semilinear numerical model, and Metcalfe *et al.* (1987), using a fully nonlinear model, observed that the transfer of energy into three-dimensional motions was slowed considerably while the large-scale vortices were merging. The stability characteristics of the flow during pairing are not accessible to standard methods of stability analysis because the two-dimensional flow is strongly time-dependent in that phase and therefore does not possess exponentially evolving normal modes. In this paper, we shall describe a straightforward extension of classical linear stability analysis which removes this difficulty and reveals the manner in which three-dimensionalization proceeds during the pairing phase. In addition, we shall extend the results of KP and PW regarding the stability of KH vortices prior to merging.

A generalization which is of obvious importance in the geophysical context is the inclusion of a background rotation $f = 2\Omega$, where Ω is the angular velocity of the reference frame. Constant rotation has no effect on a purely two-dimensional flow, but must be accounted for once three-dimensional motions are allowed. The Taylor–Proudman theorem (e.g. Greenspan 1968) predicts that sufficiently rapid background rotation will act to stabilize the two-dimensional flow against three-dimensional perturbations. The theoretical considerations of Lesieur (1991) and the large-eddy simulations of Lesieur, Yanase & Métais (1991) and Bartello, Métais & Lesieur (1994) suggest that slow rotation in the anticyclonic sense (in which the sign of f is opposite to that of the relative vorticity of the mixing layer) may destabilize the flow, while rotation in the cyclonic sense exerts a stabilizing influence. In this paper, we will compute the instability spectra in detail for various values of f and thereby provide a

full theoretical explanation of the effects that have been observed in these numerical simulations.

In addition to presenting the results of the formal stability analyses, however, we will also discuss in some detail the physical processes which drive the growth of three-dimensional perturbations. In particular, we shall focus attention on the subtle interplay of vortex tilting effects which is responsible for the elliptical instability mentioned above. These considerations will enable us to explain the spatial structure of the instability, and also to understand why it depends so crucially on the ellipticity of the streamlines. Similar mechanistic descriptions will be presented for the instability which generates streamwise vortices in the non-rotating case and for the 'edge mode', an instability which has been discovered in the course of the present work and which exists only in a rotating environment.

In §2 we briefly describe the nonlinear numerical model that has been developed to simulate the growth and pairing of two-dimensional KH vortices on an initially parallel shear layer. In this section, details of the linear, non-separable stability theory that has been devised to test the stability of these two-dimensional flows against arbitrary three-dimensional perturbations will also be presented. The theory fully allows for the possibility that the shear layer may develop in a rotating reference frame. We then discuss methods via which the perturbation equations may be cast into the form of a matrix eigenvalue problem whose solutions reveal the stability characteristics of the two-dimensional flow, even when that flow is evolving in time.

Solutions of the stability problem are presented in §§3 and 4. In §3.1, we focus on the non-rotating case. We begin by examining the stability of the two-dimensional flow at a point in its evolution just prior to the onset of pairing, thereby extending and unifying the previous results of PW and KP. We then investigate the competition between three-dimensional instabilities and the two-dimensional pairing instability by comparing the three-dimensional stability characteristics of the flow before, during and after pairing. The influence of diffusion is considered briefly in §3.2, wherein we demonstrate that the time-dependence of the background flow may impose a short-wave cutoff on the spectrum even in the absence of viscous dissipation. In §4, we investigate the effects of rotation, and compare our theoretical results with inferences based upon the recently described three-dimensional numerical simulations of Lesieur *et al.* (1991).

In §5, we discuss in detail the vortex stretching and tilting processes which drive three-dimensional instability. These considerations enable us to understand, in physical terms, several important aspects of the three-dimensionalization process. These inferences are validated by means of a quantitative analysis of the perturbation enstrophy equation. Section 6 contains a summary and concluding remarks.

2. Methodology

In this section, the analytical and numerical methods to be employed to develop and evolve a field of nonlinear, two-dimensional vortices, and to test the stability of these flows against three-dimensional perturbations will be presented. The two-dimensional numerical model that we employ for the nonlinear simulations is adapted from the model described in detail by Smyth & Peltier (1991, 1993) in previous studies of density-stratified mixing layers. The Navier–Stokes equations for two-dimensional incompressible flow are solved in the vorticity–streamfunction form:

$$\tilde{\eta}_t = \tilde{\eta}_x \tilde{\psi}_z - \tilde{\eta}_z \tilde{\psi}_x + \mathrm{D}\tilde{\eta}, \tag{1a}$$

$$\tilde{\eta} = \nabla^2 \tilde{\psi}, \tag{1b}$$

in which $\tilde{\eta}(x, z, t)$ and $\tilde{\psi}(x, z, t)$ are the two-dimensional vorticity and streamfunction fields and D is a diffusion operator. Subscripts denote partial derivatives. Note that the background rotation f has no effect on the two-dimensional flow. The initial condition consists of a mixing-layer profile of the form $\tilde{\eta} = -\operatorname{sech}^2 z$ which is perturbed by small-amplitude random noise and by a disturbance whose structure is determined by the most unstable linear eigenmode of the parallel shear flow. (While large numbers of KH vortices pair in a chaotic manner which is highly sensitive to initial conditions, the merging of one pair of vortices is a relatively simple, predictable process. Therefore, the precise form of the initial perturbation is not especially important for this two-dimensional simulation.) Lengths are scaled by the initial half-depth of the mixing layer, and times by the advective timescale. Boundary conditions are periodic in the horizontal and free slip in the vertical.

We employ the Laplacian diffusion operator $\mathrm{D} = Re^{-1}\nabla^2$, with the Reynolds number, based on half the depth of the shear layer and half the corresponding change in horizontal velocity, set at $Re = 300$. This value for the Reynolds number is typical of small-scale flows which occur in nature and in laboratory experiments. It is somewhat larger than the values employed in the three-dimensional numerical simulations of Metcalfe *et al.* (1987), Comte *et al.* (1992) and Lesieur *et al.* (1991), which become $Re = 100$, 50 and 50, respectively, when expressed in terms of our scaling.

Horizontal derivatives are evaluated in Fourier space, while vertical derivatives are computed using second-order centred differences. The advection terms are time-stepped using the leapfrog method, while a Crank–Nicholson scheme is employed for the diffusion terms. The computational domain is a square with non-dimensional length $L = 28$ on the side chosen so as to accommodate two wavelengths of the primary KH instability. To fully resolve the details of the flow, we employ 80 Fourier modes in the horizontal and 96 grid points in the vertical. The interested reader should consult Smyth & Peltier (1991, 1992) for full details regarding the two-dimensional numerical model.

We turn next to a description of the methods employed in the linear stability analysis of the two-dimensional flows that we obtain as solutions to (1). The mathematical details of this technique are by now reasonably well known, and have been described in detail elsewhere (e.g. Klaassen & Peltier 1985; KP; Smyth & Peltier 1991), and we will therefore focus here upon extensions of the technique that are being employed for the first time in the present study. The Navier–Stokes equations for three-dimensional, incompressible, rotating flow are linearized about a basic state which is independent of the spanwise coordinate y, and the perturbation is therefore assumed to vary sinusoidally in the spanwise direction, i.e.

$$\phi(x, y, z, t) = \tilde{\phi}(x, z, t) + \epsilon\hat{\phi}(x, z, t)\,\mathrm{e}^{\mathrm{i}dy}, \tag{2}$$

in which ϕ is the scalar pressure or any component of the velocity vector, d is the spanwise wavenumber and $\mathrm{i} = \sqrt{-1}$. The flow is defined with respect to a reference frame which rotates about the y-axis with angular velocity $\Omega = \frac{1}{2}f$. At $O(\epsilon)$, we obtain the following set of coupled, linear p.d.e.s for the fluctuations:

$$\hat{u}_t = -\tilde{U}\hat{u}_x - \tilde{W}\hat{u}_z - \tilde{U}_x\hat{u} - \tilde{U}_z\hat{w} + f\hat{w} - \hat{p}_x + \mathrm{D}\hat{u}, \tag{3a}$$

$$\hat{v}_t = -\tilde{U}\hat{v}_x - \tilde{W}\hat{v}_z - \mathrm{i}d\hat{p} + \mathrm{D}\hat{v}, \tag{3b}$$

$$\hat{w}_t = -\tilde{U}\hat{w}_x - \tilde{W}\hat{w}_z - \tilde{W}_x\hat{u} - \tilde{W}_z\hat{w} - f\hat{u} - \hat{p}_z + \mathrm{D}\hat{w}, \tag{3c}$$

$$0 = \hat{u}_x + \mathrm{i}d\hat{v} + \hat{w}_z, \tag{3d}$$

in which the upper case variables represent the two-dimensional fields determined by solving (1). From the geophysical perspective, our choice of coordinates is somewhat non-standard: if f represents the Earth's rotation, then our x-, y- and z-axes denote the zonal, vertical downward and meridional directions, respectively. These coordinates have been chosen for consistency with previously reported experimental and theoretical investigations of non-rotating shear layers (e.g. Orszag & Patera 1983; Corcos & Lin 1984; Bayly, Orszag & Herbert 1988). Equation (3) may be combined to form a single diagnostic equation for the pressure:

$$\nabla^2\hat{p} = f(\hat{w}_x - \hat{u}_z) - 2(\tilde{U}_x\hat{u}_x + \tilde{U}_z\hat{w}_x + \tilde{W}_x\hat{u}_z + \tilde{W}_z\hat{w}_z), \tag{4}$$

which replaces (3d). The perturbation is assumed to exhibit the same periodicity in x as does the basic state. (Note that pairing instabilities are accessible to our analyses, at least initially, since the basic state contains two wavelengths of the primary instability. The behaviour of disturbances whose wavelengths exceed twice that of the primary Kelvin–Helmholtz wave is beyond the scope of the present paper.)

Boundary conditions in the meridional direction at $z = 0, H$ are:

$$\hat{u}_z = \hat{v}_z = \hat{w} = \hat{p}_z = 0.$$

The x- and z-dependence of the problem may be represented spectrally by defining the following basis functions, which are selected so that the boundary conditions on the dependent variables will be satisfied automatically:

$$F_{\lambda\nu} = \mathrm{e}^{\mathrm{i}\lambda\alpha x}\cos \mathrm{D}_\nu z, \quad G_{\lambda\nu} = \mathrm{e}^{\mathrm{i}\lambda\alpha x}\sin \mathrm{D}_\nu z, \quad \mathrm{D}_\nu = \nu\pi/H.$$

In terms of these basis functions we may then write (employing the usual summation convection):

$$\begin{pmatrix}\hat{u}\\ \hat{v}\\ \hat{p}\end{pmatrix} = \begin{pmatrix}u_{\lambda\nu}\\ v_{\lambda\nu}\\ p_{\lambda\nu}\end{pmatrix}F_{\lambda\nu}, \quad \hat{w} = w_{\lambda\nu}G_{\lambda\nu}.$$

Applying the Galerkin formalism, we may then reduce system (3) to a set of linear o.d.e.s for which time is the independent variable. The pressure is eliminated using (4). The spanwise momentum equation (3c) decouples from the system, but will be employed later as a consistency check. The remaining equations, (3a) and (3b), may then be written in the following matrix form

$$\frac{\mathrm{d}}{\mathrm{d}t}\begin{pmatrix}u_{\kappa\mu}\\ w_{\kappa\mu}\end{pmatrix} = \begin{pmatrix}\langle UU\rangle^{\kappa\mu}_{\lambda\nu} & \langle UW\rangle^{\kappa\mu}_{\lambda\nu}\\ \langle WU\rangle^{\kappa\mu}_{\lambda\nu} & \langle WW\rangle^{\kappa\mu}_{\lambda\nu}\end{pmatrix}\begin{pmatrix}u_{\lambda\nu}\\ w_{\lambda\nu}\end{pmatrix}. \tag{5}$$

The coefficient submatrices that appear in (5) are given by

$$(1+\delta_{\mu 0})\langle UU\rangle^{\kappa\mu}_{\lambda\nu} = -\mathrm{i}\alpha\lambda\langle F^*_{\kappa\mu}\tilde{U}F_{\lambda\nu}\rangle + \mathrm{D}_\nu\langle F^*_{\kappa\mu}\tilde{W}G_{\lambda\nu}\rangle - \langle F^*_{\kappa\mu}\tilde{U}_x F_{\lambda\nu}\rangle - \frac{1+\delta_{\mu 0}}{Re}\delta_{\kappa\lambda}\delta_{\mu\nu}A_{\lambda\nu}$$
$$+\frac{2\alpha^2\kappa\lambda}{A_{\kappa\mu}}\langle F^*_{\kappa\mu}\tilde{U}_x F_{\lambda\nu}\rangle + \frac{2\mathrm{i}\alpha\kappa\,\mathrm{D}_\nu}{A_{\kappa\mu}}\langle F^*_{\kappa\mu}\tilde{W}_x G_{\lambda\nu}\rangle + f\frac{\mathrm{i}\alpha\kappa\,\mathrm{D}_\nu}{A_{\kappa\mu}}\langle F^*_{\kappa\mu}G_{\lambda\nu}\rangle,$$

$$(1+\delta_{\mu 0})\langle UW\rangle^{\kappa\mu}_{\lambda\nu} = -\langle F^*_{\kappa\mu}\tilde{U}_z G_{\lambda\nu}\rangle + \frac{2\alpha^2\kappa\lambda}{A_{\kappa\mu}}\langle F^*_{\kappa\mu}\tilde{U}_z G_{\lambda\nu}\rangle - \frac{2\mathrm{i}\alpha\kappa\,\mathrm{D}_\nu}{A_{\kappa\mu}}\langle F^*_{\kappa\mu}\tilde{W}_z F_{\lambda\nu}\rangle$$
$$+f\langle F^*_{\kappa\mu}G_{\lambda\nu}\rangle - f\frac{\alpha^2\kappa\lambda}{A_{\kappa\mu}}\langle F^*_{\kappa\mu}G_{\lambda\nu}\rangle,$$

$$\langle WU\rangle^{\kappa\mu}_{\lambda\nu} = -\langle G^*_{\kappa\mu}\,\tilde{W}_x\,F_{\lambda\nu}\rangle - \frac{2\mathrm{D}_\mu\,\mathrm{D}_\nu}{A_{\kappa\mu}}\langle F^*_{\kappa\mu}\,\tilde{W}_x\,G_{\lambda\nu}\rangle + \frac{2\mathrm{i}\alpha\lambda\,\mathrm{D}_\mu}{A_{\kappa\mu}}\langle F^*_{\kappa\mu}\,\tilde{U}_x\,F_{\lambda\nu}\rangle$$

$$-f\langle G^*_{\kappa\mu}\,F_{\lambda\nu}\rangle - f\frac{\mathrm{D}_\mu\,\mathrm{D}_\nu}{A_{\kappa\mu}}\langle F^*_{\kappa\mu}\,G_{\lambda\nu}\rangle,$$

$$\langle WW\rangle^{\kappa\mu}_{\lambda\nu} = -\mathrm{i}\alpha\lambda\langle G^*_{\kappa\mu}\,\tilde{U}G_{\lambda\nu}\rangle - \mathrm{D}_\nu\langle G^*_{\kappa\mu}\,\tilde{W}F_{\lambda\nu}\rangle - \langle G^*_{\kappa\mu}\,\tilde{W}_z\,G_{\lambda\nu}\rangle - \frac{1}{Re}\delta_{\kappa\lambda}\,\delta_{\mu\nu}\,A_{\lambda\nu}$$

$$+\frac{2\mathrm{i}\alpha\lambda\,\mathrm{D}_\nu}{A_{\kappa\mu}}\langle F^*_{\kappa\mu}\,\tilde{U}_z\,G_{\lambda\nu}\rangle + \frac{2\mathrm{D}_\mu\,\mathrm{D}_\nu}{A_{\kappa\mu}}\langle F^*_{\kappa\mu}\,\tilde{W}_z\,F_{\lambda\nu}\rangle - f\frac{\mathrm{i}\alpha\lambda\,\mathrm{D}_\mu}{A_{\kappa\mu}}\langle F^*_{\kappa\mu}\,G_{\lambda\nu}\rangle. \quad (6)$$

The inner product which appears in (6) is defined by

$$\langle\,\cdot\,\rangle = \frac{\alpha}{4\pi H}\int_0^{2\pi/\alpha}\int_0^H \cdot\,\mathrm{d}x\,\mathrm{d}z.$$

Note that if the solutions of interest had appreciable amplitude near the boundaries, the boundary conditions $\hat{p}_z = 0$ would be replaced by $\hat{p}_z = -f\hat{u}$, to take proper account of the Coriolis force. In that instance, when f is non-zero, the pressure perturbation is expanded in terms of the $G_{\lambda\nu}$ rather than the $F_{\lambda\nu}$, and the coefficients given in (6) take a slightly different form. In the present case, however, the eigenfunctions are localized far from the boundaries, so there is no appreciable difference between results obtained using $\hat{p}_z = 0$ and those obtained using $\hat{p}_z = -f\hat{u}$. For that reason, we employ (6) for both the rotating and non-rotating cases.

Note also that we have not assumed exponential time dependence, as has been done in previous studies of this kind, but rather we have left the form of the time dependence unspecified. We truncate the series expansions in accordance with the triangular scheme $2|\lambda|+\nu \leqslant N_t$ (cf. KP), and concatenate the coefficients so as to convert (5) into a standard matrix differential equation:

$$\frac{\mathrm{d}\boldsymbol{v}}{\mathrm{d}t} = \boldsymbol{A}(t)\,\boldsymbol{v}. \quad (7)$$

$\boldsymbol{A}(t)$ in (7) is an $N\times N$ full complex matrix whose time-dependence reflects the time-dependence of the two-dimensional background flow. The dimension N depends upon the degree of resolution employed in the spatial discretization process, and is equal to $N_t^2+N_t+1$. In the current calculations, N is typically of order 10^3.

If we were to employ the standard approach to such analyses, we would proceed by ignoring the time-dependence of $\boldsymbol{A}$ (or, equivalently, assume exponential time dependence in the solution) and thereby write (7) in the form of a conventional matrix eigenvalue problem, namely:

$$\sigma\boldsymbol{v} = \boldsymbol{A}(t_0)\,\boldsymbol{v}, \quad (8)$$

in which the eigenvalue σ represents an exponential growth rate. The matrix $\boldsymbol{A}$ would then be evaluated at any instant t_0 during the evolution of the two-dimensional flow, and its eigenvalues and eigenvectors computed using standard numerical methods. If a particular unstable mode that was of interest had a growth rate that was far in excess of some measure of the rate at which the background flow evolves in time, then we would argue that the neglect of the time-dependence of $\boldsymbol{A}$ was justified *a posteriori*. This

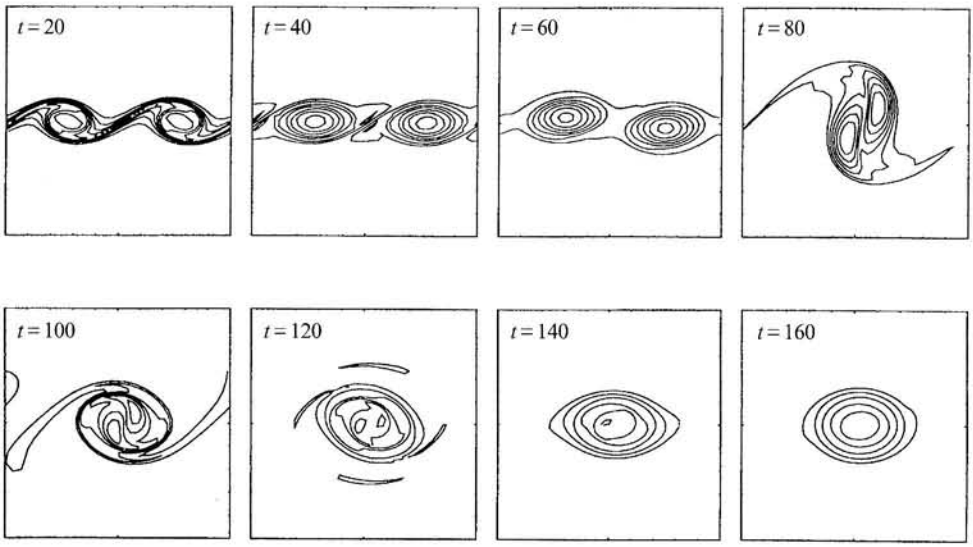

FIGURE 1. Vorticity fields for a two-dimensional, hyperbolic-tangent shear layer in a domain chosen so as to accommodate two wavelengths of the primary Kelvin–Helmholtz instability. Laplacian viscosity is employed, with $Re = 300$.

multiple-timescale approach has proved to be valid in the study of various slowly-varying flows (e.g. Smyth & Peltier 1991; KP). In the present case, however, the timescale separation argument becomes invalid during the merging phase owing to the rapid evolution of the background flow (e.g. figure 1). As a result, conclusions based on a normal mode stability analysis are likely to be misleading.

An alternative approach is simply to solve the linearized equations (7) directly as an initial-value problem (e.g. Corcos & Lin 1984; Smyth & Peltier 1990). While this approach does not depend for its validity on a separation of timescales, it is less revealing than the normal mode stability analysis in the sense that the results of a given computation pertain only to the particular initial condition selected. Since three-dimensional flows tend to be sensitively dependent on initial conditions, it is difficult to draw any general conclusions about the evolution of a generic perturbation. In contrast, the normal mode spectrum identifies the structures which are most likely to be observed, and requires only very weak constraints on the initial conditions (i.e. the initial noise field must have a non-zero projection onto a given unstable eigenmode in order for that mode to grow). In what follows, we shall describe a third approach which combines the advantages of both of the methods mentioned above.

The general solution to (7) is clearly:

$$\boldsymbol{v}(t) = \exp\left(\int_0^t A(t')\,\mathrm{d}t'\right)\boldsymbol{v}(0). \tag{9}$$

Defining the time-averaged stability matrix (TASM) corresponding to some time interval $t_1 \leqslant t \leqslant t_2$ as

$$\bar{\boldsymbol{A}}(t) = \frac{1}{\tau}\int_{t_1}^{t_2} A(t)\,\mathrm{d}t, \tag{10}$$

where $\tau \equiv t_2 - t_1$, we may write $\boldsymbol{v}_2 \equiv \boldsymbol{v}(t_2)$ in terms of $\boldsymbol{v}_1 \equiv \boldsymbol{v}(t_1)$ as:

$$\boldsymbol{v}_2 = \mathrm{e}^{\bar{A}\tau}\boldsymbol{v}_1. \tag{11}$$

To proceed, we define the eigenvalues (σ_n) and eigenvectors ($\boldsymbol{e}_n$) of the TASM through the equation:

$$\bar{\boldsymbol{A}}\boldsymbol{e}_n = \sigma_n \boldsymbol{e}_n \tag{12}$$

and write $\boldsymbol{v}_1$ as the following linear combination of the $\boldsymbol{e}_n$:

$$\boldsymbol{v}_1 = \sum_n C_n \boldsymbol{e}_n. \tag{13}$$

The solution at time t_2 may then be re-written as

$$\boldsymbol{v}_2 = \sum_n \exp(\sigma_n \tau) C_n \boldsymbol{e}_n. \tag{14}$$

In particular, if $\boldsymbol{v}_1$ is one of the eigenvectors of $\bar{\boldsymbol{A}}$ (i.e. if $C_n = \delta_{nj}$ for some j) then $\boldsymbol{v}_2$ is proportional to $\boldsymbol{v}_1$ with an amplification factor $\exp(\sigma_j \tau)$. The new method requires that we compute $\boldsymbol{A}(t)$ from the background two-dimensional flow at several points within the time interval of interest and accumulate a weighted sum which will approximate the integral in (14). In the current application, we have employed a weighted sum which corresponds to integration using the trapezoidal rule. We then carry out the eigenvalue analysis of the resulting TASM in the usual manner. In computing the TASM, we have found that evaluations of $\boldsymbol{A}(t)$ do not have to be performed at especially small intervals in time for the results to be well converged, and the method is therefore not significantly more expensive than a standard normal mode analysis. For future reference, we note that the stability matrix $\boldsymbol{A}$ is a linear function of the background velocity fields. The method described above for computing the TASM is therefore equivalent to averaging the background fields over the time interval $[t_1, t_2]$ and then computing $\boldsymbol{A}(t)$ by substituting the averaged fields into (6). If one of the eigenvectors of the TASM has a growth rate far in excess of all others, we may reasonably expect that that mode will dominate the solution $\boldsymbol{v}_2$ for a broad class of initial conditions $\boldsymbol{v}_1$. However, the validity of this assumption must be checked. Because the time interval τ is finite, and because the eigenvectors are not, in general, orthogonal, the maximally amplified disturbance will not necessarily be the dominant eigenmode but rather will be some linear combination of all of the eigenvectors. It is therefore necessary to compute this disturbance explicitly. Farrell (1989) has developed a simple method for identifying the maximally amplified disturbance in such a situation, and his method is readily adapted to the present problem.

Briefly, we define the initial and final energies

$$E_1 = \boldsymbol{v}_m^* \cdot \boldsymbol{v}_1 = \sum_{m,n} C_m^* \boldsymbol{e}_m^* \cdot \boldsymbol{e}_n C_n = \sum_{m,n} C_m^* B_{mn}^{(1)} C_n, \quad B_{mn}^{(1)} = \boldsymbol{e}_m^* \cdot \boldsymbol{e}_n,$$

$$E_2 = \boldsymbol{v}_2^* \cdot \boldsymbol{v}_2 = \sum_{m,n} C_m^* B_{mn}^{(2)} C_n, \quad B_{mn}^{(2)} = \exp((\sigma_m^* + \sigma_n)\tau) B_{mn}^{(1)},$$

in which asterisks denote complex conjugates. For this particular application of Farrell's technique, the energy norm E is just the perturbation kinetic energy. We now seek values for the C_n such that E_2 is an extremum subject to the constraint (without loss of generality) that $E_1 = 1$, and obtain:

$$\frac{\partial}{\partial C_m^*}[E_2 + \lambda(1 - E_1)] = \sum_m B_{mn}^{(2)} C_n - \lambda \sum_m B_{mn}^{(1)} C_n = 0, \tag{15}$$

λ being the Lagrange multiplier. Note that differentiation with respect to C_m rather than C_m^* in (15) simply yields the complex conjugate of the stated result, since both $B^{(1)}$ and $B^{(2)}$ are Hermitian. This property of $B^{(1)}$ and $B^{(2)}$ also guarantees that λ will be real and positive. The second equality in (15) constitutes a generalized eigenvalue problem for the C_n which may be solved using standard numerical methods. The final energy E_2 is now given by

$$E_2 = \sum_{m,n} C_m^* B_{mn}^{(2)} C_n = \lambda \sum_{m,n} C_m^* B_{mn}^{(1)} C_n = \lambda E_1.$$

The coefficients for the maximally amplified disturbance are therefore the elements of the dominant eigenvector obtained from (15). The optimization technique just described is computationally expensive, and we therefore employ it only occasionally to ensure that results obtained from the eigenanalysis of the TASM are not misleading.

In order to eliminate spurious modes which arise in consequence of the spatial discretization, we require that each accepted mode satisfy the perturbation enstrophy budget (cf. §5) to within a tolerance of 2%. We have found that this procedure eliminates spurious modes while retaining those which are physically relevant. Additional consistency checks are performed using the spanwise momentum equation (3*b*) and the perturbation kinetic energy equation.

Our choice of flow diagnostics in the analyses to follow is governed by the desire to understand the characteristics of the unstable modes in detail while still covering a large region of parameter space in an efficient manner. Therefore, we shall calculate at each phase of flow evolution the growth rates of the dominant modes as functions of the spanwise wavenumber d and also perturbation kinetic energy, spanwise velocity and spanwise vorticity fields corresponding to modes which are of particular interest. An additional diagnostic that has proved extremely useful in enhancing understanding of the physical mechanism of three-dimensional instability is the above-mentioned perturbation enstrophy budget. This diagnostic will be described fully in §5.

3. The non-rotating case

In this section, we shall discuss the stability characteristics of a two-dimensional shear layer for the special case $f = 0$. In §3.1, we focus upon the flow described in §2, which evolves under the action of Laplacian diffusion with $Re = 300$. We investigate the susceptibility of the flow to three-dimensional perturbations before, during and after the KH vortices merge. In §3.2, we replace the Laplacian diffusion with a high-order hyperviscous operator, thereby rendering the model effectively inviscid, and briefly investigate the effect that this has on the short-wave cutoff exhibited by the instability spectrum.

3.1. *Non-rotating, viscous flow*

In figure 1, we display contour diagrams of the vorticity field computed at the non-dimensional times $t = 20, 40, 60, \ldots, 160$, from the two-dimensional simulation with $Re = 300$. The primary KH instability grows rapidly, and the subharmonic becomes visible at $t = 60$. From $t = 60$ to $t = 100$, vortex merging and the accompanying filamentation (e.g. Melander, Zabusky & McWilliams 1988) are clearly visible. At $t = 100$, we observe a single vortex structure within which the remnants of the primary vortices remain visible. These features subsequently diffuse, leaving behind a single elliptical vortex. This feature is, of course, one member of a periodic train of quasi-isolated vortices which are prevented from further merging by the boundary conditions.

The time-evolution of the vortex state during this phase consists of slow viscous diffusion plus a slight nutation due to the influence of the neighbouring vortices. We terminate the simulation at this point because a second pairing would by now be underway if the boundary conditions permitted it.

We turn now to the analysis of the stability of the evolving two-dimensional KH wavetrain shown in figure 1 to small-amplitude, three-dimensional perturbations. Because our experiments are performed on a computational domain which contains two wavelengths of the primary KH wave, the secondary stability analyses deliver unstable modes whose streamwise wavelength is the same as the primary wave (longitudinal instabilities) and also those whose wavelength is double that of the primary wave (subharmonic instabilities). We will find it convenient to denote these instabilities by the symbols $\{L_n, n = 1, 2, \ldots\}$ and $\{S_n, n = 0, 1, 2, \ldots\}$, respectively. In previous studies (PW; Klaassen & Peltier 1989; Smyth & Peltier 1993), the latter class of modes was computed separately using Floquet theory. The disadvantage of the present approach is that the enlarged spatial domain is more difficult to resolve using finite computational resources. Resolution tests have shown that setting $N_t = 37$ is more than sufficient to obtain convergence in the secondary stability analysis at $t = 40$, and we have used this value in all of the calculations pertaining to that case. At later times in the evolution of the KH wavetrain, the eigenfunctions exhibit decreased levels of small-scale structure and are therefore more easily resolved. For those cases, we set $N_t = 31$.

In what follows, we shall find it useful to distinguish three time intervals: respectively the pre-pairing, pairing, and post-pairing phases. From $t = 30$ to $t = 50$, the KH wave pair evolves relatively slowly. During this time, the subharmonic is adjusting its phase relationship with the primary KH wavetrain in order that it may grow and cause the primary vortices to merge (Klaassen & Peltier 1989; Smyth & Peltier 1993). During this time, the unstable modes have relatively large growth rates, and timescale separation may therefore be invoked in order to justify 'freezing' the flow at a particular point in time and analysing its stability as though it were a steady state (cf. (8) and the accompanying discussion). The stability characteristics of the KH wavetrain at this point in its evolution have been discussed previously by KP, although only the longitudinal modes (and the influence of stable stratification upon them) were considered in that study. While it would be logical to base the stability analysis on a calculation of the eigenmodes of the TASM (see §2) defined on, say, the time interval $30 \leqslant t \leqslant 50$, we perform the analysis instantaneously at $t_0 = 40$ in order that we may readily compare our results with those obtained previously by KP. This approach is justifiable in the light of the slow evolution of the KH wavetrain prior to pairing. The remaining quantitative differences between KP's results and ours are due to the fact that our background flow at $t = 40$ does not correspond exactly to the maximum-amplitude state whose stability was analysed in the former study.

The pairing phase will be defined as the time interval between $t_1 = 60$ and $t_2 = 100$. During this phase, the flow evolves rapidly and the stability analysis is therefore performed using the new 'TASM' method described in the previous section. We define the post-pairing phase as extending from $t_1 = 100$ to $t_2 = 140$. Although the background flow evolves much more slowly in the post-pairing phase than in the pairing phase, we shall again employ the TASM method in performing the stability analyses. Direct comparisons between instantaneous stability analyses and those performed using the TASM method will be presented in §3.2 in the context of a discussion of viscous effects.

In figure 2, we plot the growth rates of the five most unstable modes of the KH

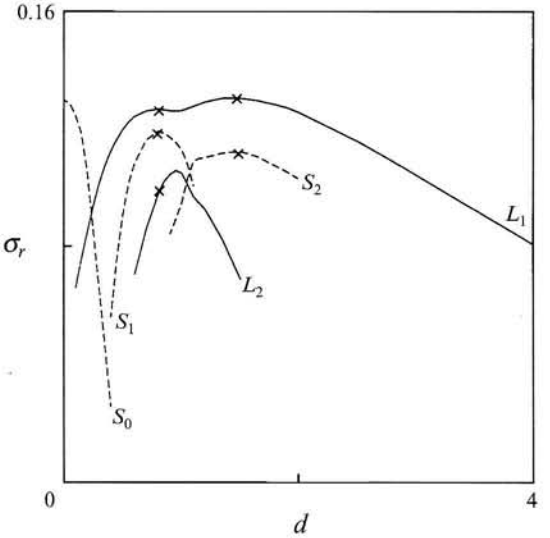

FIGURE 2. Instantaneous secondary instability spectrum for the non-rotating Kelvin–Helmholtz wavetrain at $t = 40$ (just prior to pairing). ——, longitudinal modes; – – –, subharmonic modes. ×, modes whose spatial structures are to be displayed in figures 3 and 4.

vortex, analysed at $t = 40$, as a function of the spanwise wavenumber d. Solid (dashed) curves represent longitudinal (subharmonic) modes. The leftmost dashed curve represents the well-known pairing instability, which we shall denote by the symbol S_0. The pairing mode has been described in detail by PW (using the Stuart vortex as a background flow) and by Klaassen & Peltier (1989) and Smyth & Peltier (1993) (using numerically-evolved KH wave states and also investigating the effects of stable stratification), and we will therefore not discuss it in detail in the present paper. The helical pairing instability, as this was defined by PW, is just the extension of the transverse ($d = 0$) pairing mode to non-zero (but small) spanwise wavenumbers. The second dashed curve in figure 2 represents mode S_1, a subharmonic instability similar to the helical pairing mode, whose existence has not previously been noted. The S_1 mode is more helical than the S_0 mode, and exhibits a growth rate which is only slightly smaller. The S_2 mode is a second new subharmonic mode; its properties will be discussed below. The uppermost solid curve in figure 2 corresponds to the longitudinal mode L_1, which is the dominant mode of KP's principal spectrum. This mode is denoted ω_0 in KP's nomenclature and is identified by a diamond symbol in their figure 13. The remaining solid curve represents a second longitudinal mode, denoted L_2, which was identified by KP as PW's translative mode. The modes whose growth rates are shown in figure 2 are all stationary (i.e. their growth rates are purely real), and comprise the entire set of modes whose growth rates exceed 0.10 for some value of d at this particular point in the flow evolution.

Throughout this investigation, we have found (as did KP) that unstable modes tend to occur in harmonic sequences. Such a sequence consists of a set of modes with oscillation frequencies $\sigma_{in} \approx n\sigma_{i1}$; $n = 0, 1, 2, \ldots$, where σ_{i1} is the fundamental frequency. The growth rate σ_r generally decreases with increasing n, so that the stationary mode with $n = 0$ is the most unstable. While σ_r is usually a strong function of spanwise wavenumber, as is illustrated in figure 2, σ_i tends to vary very little over large ranges of d. In view of these observations, we shall focus our attention on the

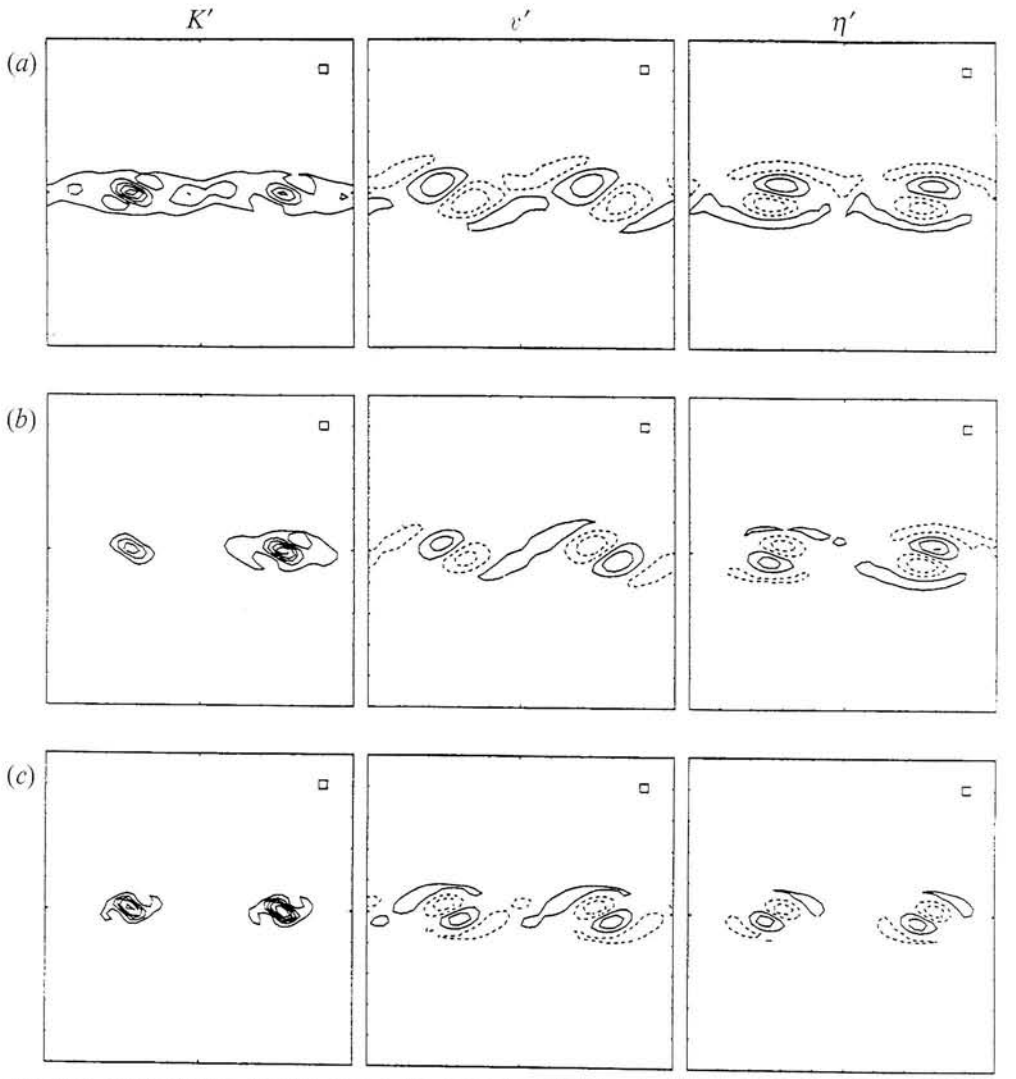

FIGURE 3. Perturbation kinetic energy K', spanwise velocity v' and spanwise vorticity η' fields for the three most unstable modes of the wavetrain at $t = 40$ with $d = 0.8$, $f = 0$.

$n = 0$ modes, occasionally noting the fundamental frequencies σ_{i1} of the associated harmonic sequences.

In figures 3 and 4, we display the spatial structures of the most unstable modes at $d = 0.8$ and $d = 1.5$, respectively, as revealed by the kinetic energy K', the spanwise velocity v' and the spanwise vorticity η' associated with each mode. The perturbation kinetic energy is quadratic in the disturbance fields and is therefore averaged over a single spanwise wavelength to give a positive, real function of x and z. The spanwise velocity and vorticity perturbations vary sinusoidally with y, and each of these diagrams shows the corresponding field evaluated on a plane of constant y which has been chosen to coincide roughly with the antinode of the y-dependent oscillation. The modes shown in figure 3 are all core-centred, i.e. the K' fields are largest near the cores of the primary KH vortices. The L_1 mode at $d = 0.8$, shown in figure 3(*a*), clearly corresponds to PW's translative instability: the η' field describes a translation of each KH vortex upward and to the right (or to the northeast, in the geophysical context).

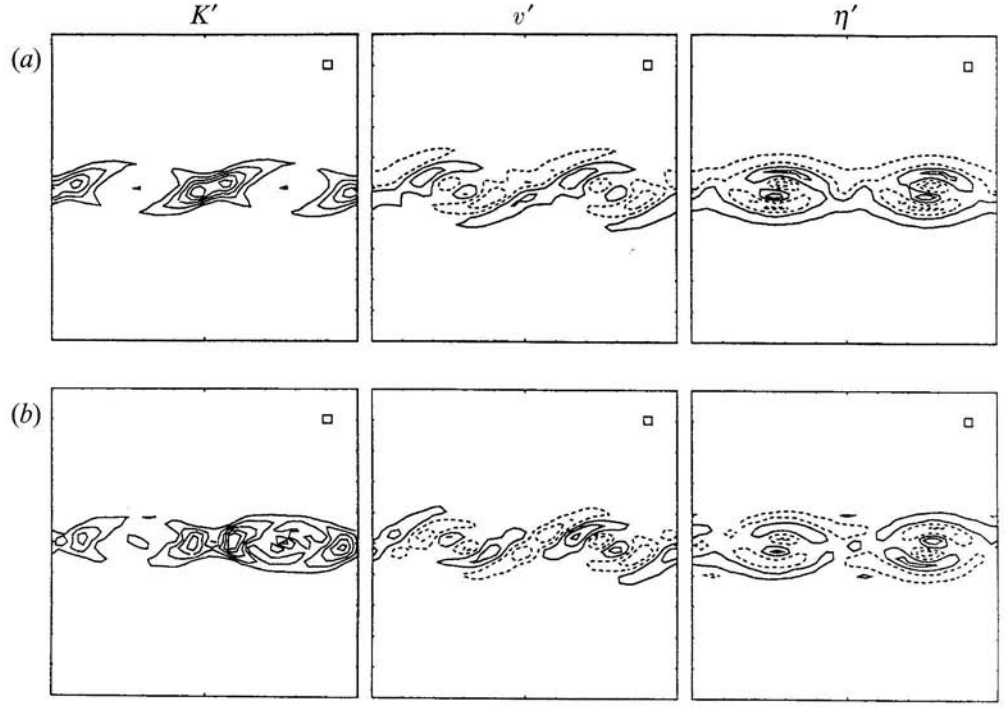

FIGURE 4. Perturbation kinetic energy K', spanwise velocity v' and spanwise vorticity η' fields for the two most unstable modes of the wavetrain at $t = 40$ with $d = 1.5, f = 0$.

The S_1 mode (figure 3*b*) exhibits approximate antisymmetry about the stagnation points which lie between the KH vortices. As a result, the translations of adjacent vortex cores are 180° out of phase, and the result is a helical pairing motion similar to that described by PW. Note that, unlike PW's helical pairing mode, this mode is not contiguous with any mode which exists in the limit $d \to 0$. The new mode is most unstable at $d = 0.8$, which corresponds to a spanwise wavelength slightly greater than half the wavelength of the primary KH wavetrain. This mode therefore acts to promote the formation of a diamond pattern of interlocking vortex tubes whose aspect ratio is of order unity (see figure 6 of PW). The L_2 mode (figure 3*c*) again corresponds to translative instability. It differs from the mode shown in figure 3(*a*) only in its smaller growth rate and in the fact that it is somewhat more strongly core-centred.

Pierrehumbert (1986; see also Bayly 1986) has shown that any region in which the streamlines of the background flow are approximately elliptical (and the vorticity is approximately constant) will support a three-dimensional instability that has come to be known as elliptical instability. It is of interest to compare the characteristics of the core modes discovered here (i.e. L_1, S_1 and L_2) with those predicted on the basis of Pierrehumbert's idealized model. Comparison of the perturbation spanwise vorticity fields displayed in figure 3 with those shown in figure 2 of Pierrehumbert (1986) reveals that the spatial structure of our core modes is very consistent with the structure predicted for elliptical instability. Quantitative comparison of growth rates is difficult to perform with precision, because the growth rate of the elliptical instability scales with the value chosen for the 'constant' vorticity of the core, which in real situations must be some arbitrarily defined average value. In addition, since our streamlines are not perfect ellipses, the value chosen for the 'ellipticity' of the core is also somewhat arbitrary. Taking the ellipticity of our vortex core to be 0.25 and the characteristic non-

dimensional vorticity in the core to be 0.8, we predict using Pierrehumbert's results a growth rate $\sigma = 0.08$. Our core modes exhibit growth rates ranging from zero to about 0.13. This level of agreement is satisfactory given the approximations made, and we conclude that all of the core modes are essentially manifestations of elliptical instability. This conclusion will be supported further in §5.1, where we will elucidate the physical mechanism of elliptical instability, and show that the core modes encountered here grow as a consequence of that mechanism.

In figure 4, we display the spatial dependences of the two most unstable modes at spanwise wavenumber $d = 1.5$. This is the value of d at which the most unstable three-dimensional mode (L_1) is found. This mode, shown in figure 4(*a*), is concentrated in the strained regions, or braids, located between the KH vortex cores, and clearly corresponds in terms of its spatial morphology to the dominant mode of KP's principal spectrum. Inspection of the spanwise velocity diagram reveals that this mode promotes the formation of counter-rotating vortex tubes whose axes are aligned roughly perpendicular to the axes of the primary KH vortices. It is therefore clear, as was proposed by KP, that this mode is responsible for the rib structures which have been observed in the laboratory experiments of Breidenthal (1981), Bernal & Roshko (1986), Lasheras *et al.* (1986) and Lasheras & Choi (1988), and in the numerical simulations of Metcalfe *et al.* (1987). It now seems clear that the distinction between this mode and PW's translative mode may be misleading, since the two modes are contiguous members of the L_1 branch. Upon inspection of figure 2, the reader will note that the $\sigma(d)$ curve corresponding to the dominant longitudinal mode L_1 exhibits a slight kink near $d = 0.9$. Detailed analyses have revealed that the spatial form of the L_1 mode changes rather abruptly at this point, from the core-centred structure in figure 3(*a*) to the brain-centred disturbance shown in figure 4(*a*). We note that remnants of the core-centred structure are visible in the η field in figure 4(*a*). KP investigated the spatial structure of each mode only for the spanwise wavenumber d at which the growth rate is a maximum. In consequence, the correspondence at $d < 0.9$ between the L_1 mode and the translative instability is not evident in KP's results.

The S_2 mode (figure 4*b*) is again concentrated on the braids of the KH vortices. Like the L_1 mode, it tends to produce vortex tubes aligned perpendicular to the large vortices, but in this case the secondary vortex tubes found at the same spanwise location on adjacent KH vortices rotate in opposite directions. Unlike the L_1 mode, the S_2 mode is not contiguous with its low-wavenumber counterpart, the helical pairing mode S_1, but the relationship between the spatial structures is clearly similar.

Having established the stability characteristics of the KH wavetrain in the pre-pairing phase, we now turn our attention to the pairing phase, which extends from $t = 60$ to $t = 100$. We have performed instantaneous stability analyses at numerous times within this interval, and have found that the growth rates of the secondary instabilities are much smaller than those which obtain prior to pairing. At $t = 60$, at which point the adjacent KH vortices are just beginning to orbit each other (cf. figure 1), the instabilities illustrated in figures 2–4 are still easily identified, but by $t = 70$ those modes have been almost entirely stabilized, and are replaced by a qualitatively different set of modes whose growth rates are smaller by roughly a factor of two. These new modes correspond to the longitudinal modes of the emerging subharmonic KH vortex, as we shall show. Because the normal modes grow relatively slowly during pairing, and because the background flow evolves quickly, the results of the instantaneous stability analyses are of dubious validity. The *e*-folding time of a typical unstable mode during this phase is $\Delta t = 16$, during which time the structure of the background flow is substantially altered (cf. figure 1). It is in response to this problem that we have

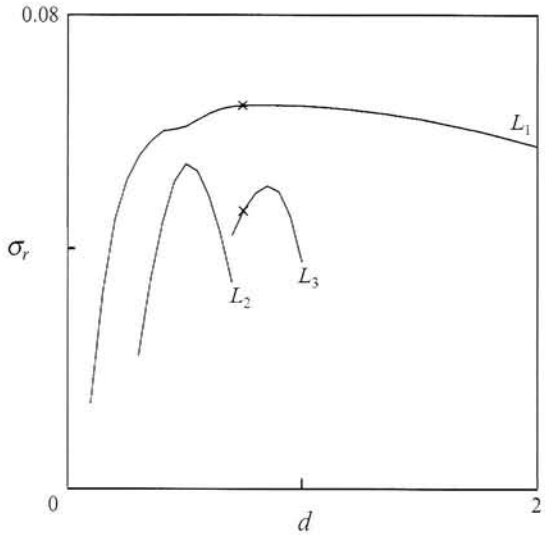

FIGURE 5. Instability spectrum for the non-rotating Kelvin–Helmholtz wavetrain during the pairing phase $60 \leqslant d \leqslant 100$.

developed the more rigorous TASM method of stability analysis described in §2, which we now employ. The stability matrix $\boldsymbol{A}(t)$ is obtained using previously-calculated two-dimensional flow fields at times $t = 60, 65, 70, \ldots, 100$, and summed in the appropriate fashion to form the TASM.

Figure 5 shows the growth rate spectra of all modes for which $\sigma(d)$ exceeds 0.05 for some d. These spectra are determined by the eigenvalues of the TASM averaged over the time interval $60 \leqslant t \leqslant 100$. The maximum growth rate observed is 0.064, roughly half the maximum growth rate which obtains in the pre-pairing phase. In figure 6, we display the eigenfunctions of the two most unstable modes at $d = 1$. Comparison with figures 3 and 4 reveals that these modes are just the longitudinal modes identified previously, but they are now properties of the subharmonic KH vortex (cf. figure 1) as opposed to the primary vortices. The most unstable mode shown in figure 5 is core-centred at small d and braid-centred at large d, and we therefore identify it as the longitudinal mode L_1. The two weaker modes are core-centred, and we identify them as L_2 and L_3, as indicated on figure 5.

As was noted in §2, the TASM describes disturbance evolution over a finite time interval, and its eigenmodes are in general not orthogonal. Therefore, there is no *a priori* justification for restricting our attention to the eigenmodes of the TASM as we search for the disturbance which amplifies optimally over the time interval $60 \leqslant t \leqslant 100$, and the identification of that disturbance with the most unstable eigenmode (cf. figure 6) may be misleading. To test this possibility, we have taken $d = 1$ as the most probable value for the spanwise wavenumber of the optimally amplified disturbance (cf. figure 5), and computed that disturbance explicitly using the 'optimal instability' method described in §2. The result is displayed in figure 7. Figures 7(*a*) and 7(*b*) show the spatial structure of the optimally-growing disturbance at $t = 60$ and $t = 100$, respectively. Between these times, the perturbation kinetic energy K' increases by a factor of 346, which corresponds to an average exponential growth rate $\sigma = 0.0731$. This value is indeed substantially in excess of the growth rate of the most unstable eigenmode, which is $\sigma = 0.0645$ and which leads to an energy amplification factor of 174.

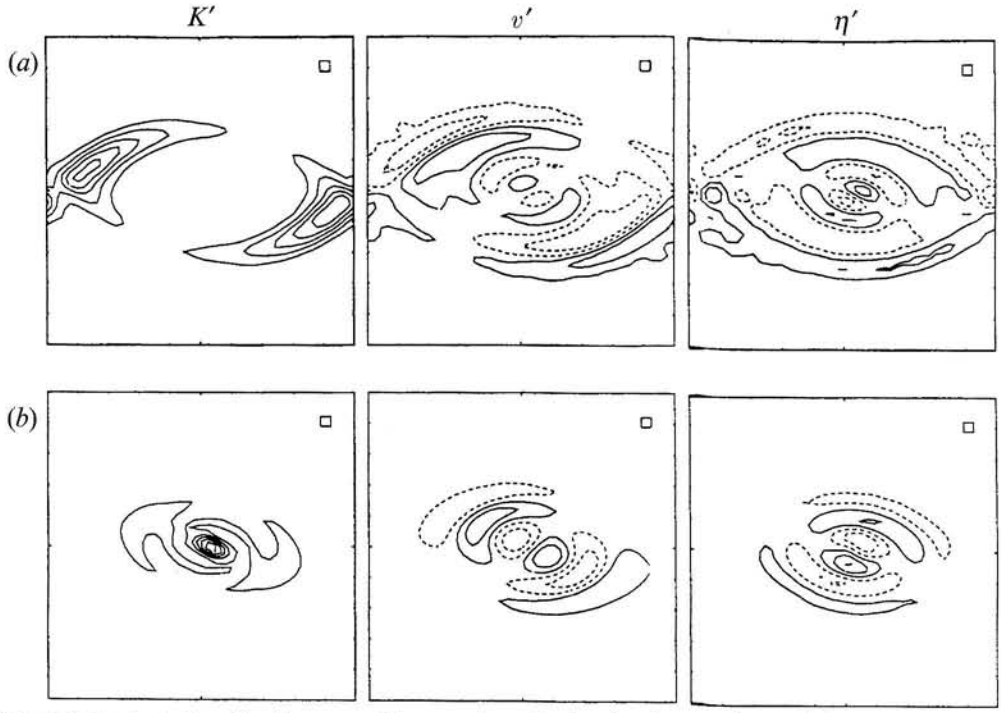

FIGURE 6. Perturbation kinetic energy K', spanwise velocity v' and spanwise vorticity η' fields for the two most unstable modes of the Kelvin–Helmholtz wavetrain during the pairing phase, with $d = 1.0$, $f = 0$.

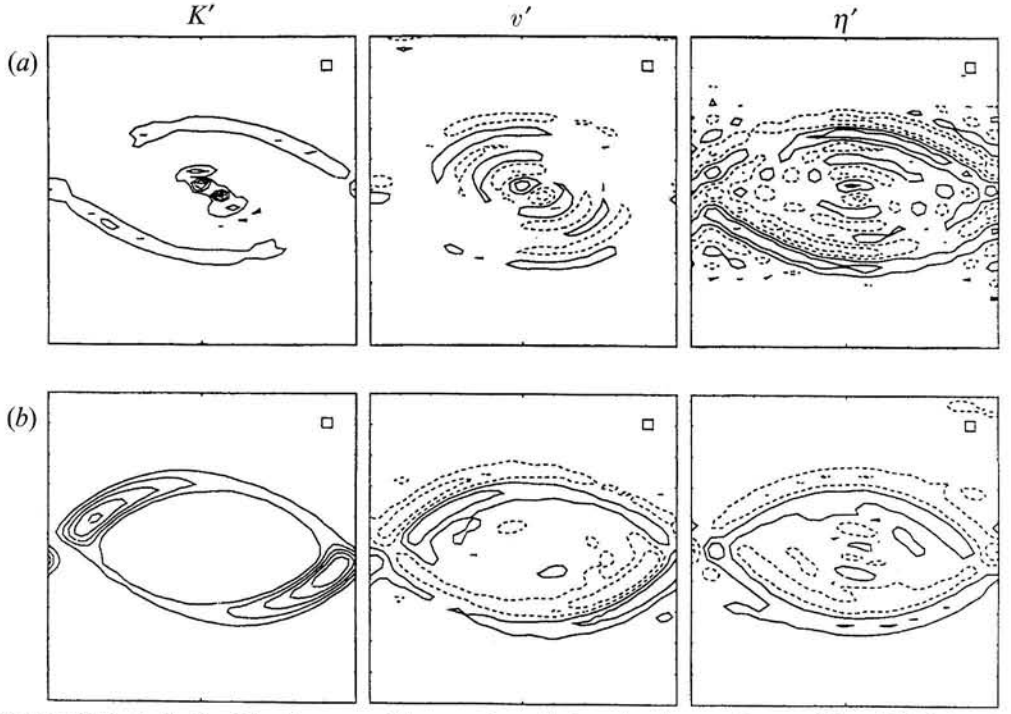

FIGURE 7. Perturbation kinetic energy K', spanwise velocity v' and spanwise vorticity η' fields for the disturbance which amplifies maximally during the pairing phase, shown (*a*) at $t = 60$, (*b*) at $t = 100$.

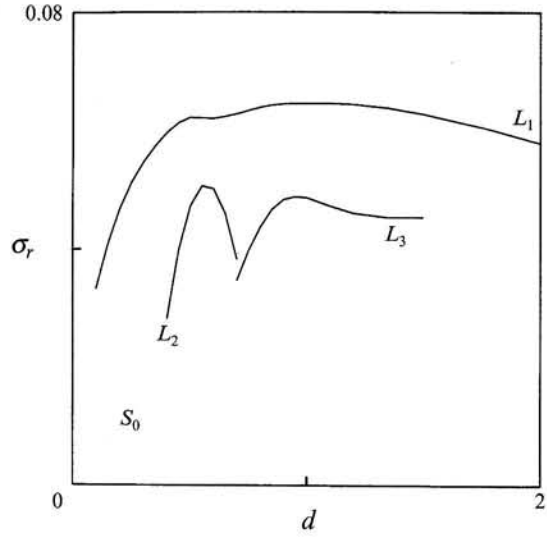

FIGURE 8. Instability spectrum for the non-rotating Kelvin–Helmholtz wavetrain during the post-pairing phase $100 \leqslant d \leqslant 140$.

The optimal disturbance, shown in figure 7(*a*), exhibits a preponderance of small-scale structure (this is a common property of optimally amplified disturbances; see Farrell 1989 for examples). This makes spatial resolution a problem, and it is clear that the structure shown in figure 7(*a*) is not particularly well resolved. Unfortunately, this computation requires twice as much core memory as does the eigenvalue analysis of the TASM, and the truncation level $N_t = 31$ is therefore the largest value accessible to us at present. However, test calculations performed using $N_t = 19$, 23, 27 and 31 have shown that both the amplification factor and the structure of the K' field are well converged at $N_t = 31$, and that the qualitative features of the v' and η' fields are consistent over this range of truncation levels. It therefore appears that the use of finer spatial resolution would not alter the results significantly. The K' and v' fields are strongest at the core of the subharmonic KH vortex, while the spanwise vorticity perturbation η' is maximized on the edges of the vortex. The final form of the disturbance, shown in figure 7(*b*), is markedly different from the initial form, indicating that this disturbance contains a mixture of components proportional to different eigenmodes of the TASM. However, the final form is very similar to the most unstable eigenmode (cf. figure 6*a*). The optimally amplified disturbance is strongly braid-centred at the completion of pairing, and has clearly developed into the rib-like structures which have been observed in the experimental and numerical investigations cited above. We conclude that the results of the eigenanalysis of the TASM yields accurate information, at least in the present application, regarding the most probable evolution of small-amplitude disturbances on this strongly time-dependent background flow.

We conclude this section by examining the three-dimensional secondary instabilities of the two-dimensional KH wavetrain in the post-pairing phase, i.e. in the time interval $100 \leqslant t \leqslant 140$. The growth rates of the dominant eigenmodes of the TASM are shown in figure 8. Comparison of this result with that illustrated in figure 5 reveals that the post-pairing spectrum is very similar to that obtained during the pairing phase. The spatial structure of the dominant eigenmode will be described in detail in the following

section (cf. figure 14*b*); for the present we note that the eigenmode is also nearly identical to the dominant mode found during the pairing phase. We therefore conclude that the stability characteristics of the pairing phase are already dominated by the spectrum associated with the emerging subharmonic vortex.

The axes on figure 8, as well as those on figure 5, have been deliberately rescaled by a factor of $\frac{1}{2}$ with respect to figure 2, so that the reader may easily compare the growth rates of the longitudinal modes of the paired vortex state, and the spanwise lengthscales at which they occur, with corresponding quantities which obtain for the primary KH vortices prior to pairing. Such a comparison reveals that there is a strong degree of self-similarity in the spectra of the pre-pairing and post-pairing states. The self-similarity of the two-dimensional pairing process is manifested in the fact that the depth of a mixing layer grows linearly in time (Lesieur *et al.* 1988; Smyth & Peltier 1993), or in space in the case of a spatially-growing layer (e.g. Brown & Roshko 1974). One may speculate that, to the degree that three-dimensional perturbations evolve, like the pairing process, on the advective timescale which is established by the large-scale shear, their linear growth rates and spanwise wavenumbers should exhibit the same temporal and spatial self-similarity. The present results provide substantial confirmation of this hypothesis.

The most obvious departure from self-similarity is found in the spanwise lengthscale of the most unstable three-dimensional mode. The growth rate is a maximum at $d = 1.5$ prior to pairing and at $d = 1.0$ after pairing. There are two reasons for this discrepancy. Firstly, the stabilization of small-scale modes is controlled largely by viscous processes, rather than by the advective dynamics of the two-dimensional vorticity distribution, and it therefore obeys different scaling laws. Secondly, note that the pre-pairing phase was analysed instantaneously at $t = 40$ (for comparison with KP), whereas the stability characteristics of the post-pairing phase were computed using the TASM (despite the fact that the background flow evolves on a slow timescale during that phase). The influence of viscosity and of time-dependence in the background flow will be discussed in the following subsection.

3.2. *The effects of diffusion*

In several previous investigations of secondary instabilities (PW; Orszag & Patera 1983; Pierrehumbert 1986; Smyth & Peltier 1991), it has been observed that growth rates of secondary instabilities may increase monotonically with increasing spanwise wavenumber. The extent of this monotonic increase, which we refer to as an 'ultraviolet catastrophe', is limited only by the viscosity-imposed short-wave cutoff, and the phenomenon is therefore interpreted as a direct transfer of energy into the viscous subrange. These observations have important implications for our understanding of turbulent dynamics (e.g. Pierrehumbert 1986).

An example of this ultraviolet catastrophe is provided by the solid curve in figure 9. To compute this result, we first re-created the two-dimensional simulation previously illustrated in figure 1, this time replacing the Laplacian viscosity operator in (1*a*) with a hyperviscous operator of the form $\mathrm{D} = R^{-1}\nabla^8$. The constant R was set to the value 1.5×10^7. The resulting two-dimensional evolution (which we shall not illustrate here) is qualitatively very similar to that shown in figure 1, except that the end state vortex exhibits in profile a somewhat flatter core, and the filaments of strong spanwise vorticity which are formed during pairing persist for much longer than they do in the viscous case (as do the small-scale features within the core of the end-state vortex). We then performed a three-dimensional stability analysis instantaneously at $t = 120$ (see figure 1 for an approximate picture of the flow at this point), making the appropriate

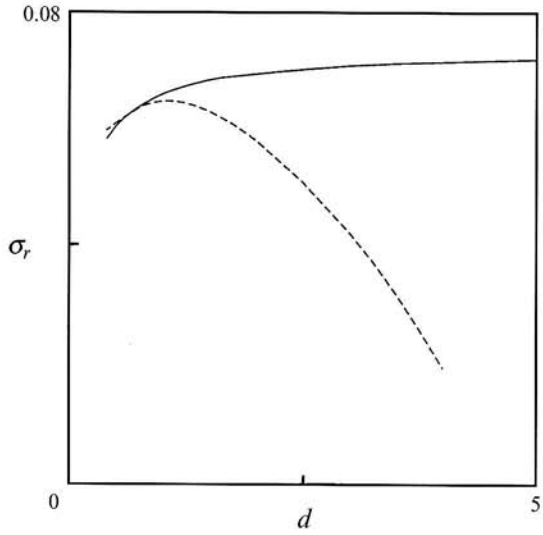

FIGURE 9. Growth rate versus spanwise wavenumber for the post-pairing case, computed using hyperviscosity. Curves correspond to the L_1 mode. Stability analyses are performed ——, instantaneously at $t = 120$ and – – –, over the time interval $100 \leqslant t \leqslant 140$ using the TASM method.

modifications to the viscous terms in (6). The dominant instability is, as usual, the L_1 mode, whose energy is focused in the core for small d, in the braids for large d. As is clear upon inspection of the solid curve in figure 9, the effective removal of viscosity from the model allows the growth rate of the dominant L_1 mode to increase monotonically with increasing d. Further calculations, performed using spanwise wavenumbers up to $d = 10$, have shown that the growth rate continues to increase, asymptoting to a limiting value slightly in excess of 0.08. (It must be noted that our spatial resolution is questionable for these very large values of d. However, there is an apparently-universal tendency for large-d modes to appear more unstable as resolution is increased, so we expect that calculations performed using higher resolution would, if anything, show an even greater tendency for σ to increase with d.) This behaviour might be taken to suggest that the L_1 mode is capable of transferring energy into a broad range of spanwise lengthscales which extends to the dissipation scale.

Given the slowness of the fluctuations in the two-dimensional flow at this point in its evolution, one would expect that the instantaneous stability analysis described above would be justified in terms of timescale separation, and that its results would accurately reflect the stability characteristics of the flow during the post-pairing phase. As a check on this assumption, we repeated the stability analysis of the post-pairing phase using the TASM method and averaging the background flow over the time interval $100 \leqslant t \leqslant 140$, as was done in §§3 and 4. The corresponding result is shown by the dashed curve in figure 9. There is little difference between the two curves at low d, but we now observe a distinct short-wave cutoff at high d. Calculations like those just described have also been performed for the pre-pairing phase, and the results have been the same: the ultraviolet catastrophe is no longer observed when the time-dependence of the background flow is accounted for using the TASM method, even though the model is effectively inviscid.

We therefore conclude that even a slow time dependence in the two-dimensional background flow may act to decorrelate small-scale modes, and may therefore impose a short-wave cutoff independently of the action of viscosity. In other words, the direct

transfer of energy to arbitrarily small scales of motion may be possible only when the background flow is precisely in equilibrium.

4. The rotating case

We turn now to an investigation of the effect of rotation on the stability characteristics of the two-dimensional flow. As in §3.1, we assume Laplacian diffusion with $Re = 300$. The rotation has angular frequency $\Omega = \frac{1}{2}f$, f being the associated vorticity. The rotation vector points in the y-direction, so that the background vorticity represented by f is aligned with the vorticity field of the two-dimensional flow. The Taylor–Proudman theorem (e.g. Greenspan 1968), stated loosely, suggests that rotating flows will tend to be two-dimensional, or (in the language of the present paper) that rotating two-dimensional flows tend to be stable against three-dimensional disturbances, provided that the ambient rotation is sufficiently rapid. In the present case, any three-dimensional circulations that may evolve, particularly those which are concentrated near the vortex cores, develop in a flow that is strongly rotational even if $f = 0$. When f is positive, the rotation of the reference frame adds vorticity that has the same sign as the relative vorticity $\tilde{\eta}(x, z)$, and therefore the three-dimensional motion will be subject to the influence of effectively enhanced rotation. In consequence of this, we expect positive ambient rotation to have a stabilizing effect. However, when f is negative, the shear layer is located in a reference frame which is rotating in a sense that is opposite to its own relative vorticity, which means that the absolute vorticity $f+\tilde{\eta}(x, z)$ is closer to zero than is the relative vorticity $\tilde{\eta}(x, z)$. We might therefore expect that small negative values of f will tend to render the flow less stable against three-dimensional fluctuations. Lesieur 91991, §3.3.1) has further suggested that regions of the two-dimensional flow in which $\tilde{\eta}+f$ is close to zero should be more susceptible to three-dimensional instability than regions in which $\tilde{\eta}+f$ is far from zero. In what follows, it will be seen that the results of our stability analyses not only provide strong support for these qualitative ideas, but also demonstrate that a new and particularly dangerous mode of three−dimensional destabilization dominates in the region of small negative f.

The detailed stability analysis for the case of rotating flow may be performed using the same two-dimensional simulations that were employed in the non-rotating cases, since f has no effect on a two-dimensional flow. We will not display results pertaining to the pre-pairing, pairing and post-pairing phases separately, but will rather focus upon the post-pairing phase. There will be no significant loss of generality because of this, since the relationships among the instability spectra which obtain during the different time intervals is simple and has been described in detail in the previous section. Explicit studies of the pre-pairing phase, in which two KH vortices are present, have shown that modes tend to appear in pairs with nearly equal growth rates. In each pair, one mode is concentrated near each of the two KH vortices. As a result, each mode may occur with equal probability in longitudinal form, in subharmonic form, or in any combination of the two. By focusing on the post-pairing phase, in which only one KH vortex is present, we avoid the unnecessary complication of dealing simultaneously with longitudinal and subharmonic modes. Note, however, that the assumption that the flow remains essentially two-dimensional at large scales may be less defensible in the rotating case than in the non-rotating case. Johnson (1963) and Yanase *et al.* (1993) have shown that a rotating shear layer exhibits three-dimensional primary instabilities whose growth rates exceed that of the primary KH instability. Nevertheless, we assume that a vortex in a rotating reference frame may evolve to finite

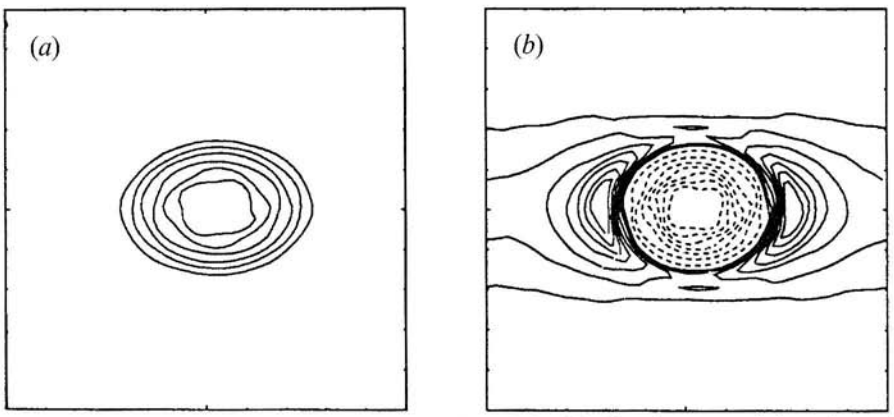

FIGURE 10. (*a*) The temporally averaged background vorticity field for the post-pairing phase. (*b*) The squared eigenvalue s^2 of the strain tensor (cf. 16) for the background field shown in (*a*). The spacing of the dashed contours, which denote negative values of s^2, is larger than the spacing of the solid contours by a factor of 3.4.

amplitude while remaining essentially two-dimensional. The validity of our conclusions will be tested by means of a comparison with the numerical simulations of Lesieur *et al.* (1991), in which the flow had access to all three spatial dimensions from the outset.

The relative vorticity field $\tilde{\eta}$, averaged over the time interval $100 \leqslant t \leqslant 140$, is shown in figure 10(*a*). In figure 10(*b*), we show the spatial distribution of the squared eigenvalue of the deformation tensor $\partial \tilde{U}_i / \partial x_j$, namely:

$$s^2 = \tilde{U}_z \tilde{W}_x - \tilde{U}_x \tilde{W}_z, \tag{16}$$

which corresponds to the vorticity field shown in figure 10(*a*). In regions of positive s^2, the flow consists primarily of a straining deformation and neighbouring Lagrangian trajectories diverge exponentially along the principal axis of positive strain. It is in these regions that the downscale cascades associated with two-dimensional turbulence are most active (e.g. Smyth 1992). Three-dimensional instability is also expected to be important in these regions in light of the remarks of Lesieur *et al.* (1988), who showed that three-dimensional motions may be connected with the growth of error (i.e. the divergence of nearby parcel trajectories) in the two-dimensional flow. In regions where $s^2 < 0$, the flow is essentially rotational, and neighbouring trajectories do not diverge (McWilliams 1984; Weiss 1991).

In previous studies (e.g. Lesieur *et al.* 1991), the rotation rate has been expressed in terms of a Rossby number R_0, which is the ratio of some characteristic measure of the relative vorticity of the two-dimensional flow to the ambient vorticity f. In our studies of the post-pairing phase, we find that the maximum vorticity, which occurs in the core of the KH vortex, has the value 0.77. The appropriate Rossby number is therefore $R_0 = 0.77/|f|$.

The solid curve in figure 11 denotes the growth rate of the most-unstable mode of the post-pairing regime ($d = 1$) as a function of f. For $f > 0$, the mode is rapidly stabilized. For $f < 0$, we observe a small range of stabilization centred near $f = -0.07$, followed by two ranges in which the instability again achieves substantial growth rates. Near $-f = 0.35$, the growth rate reaches a maximum value of 0.083, an increase of 28% over the value obtained in the non-rotating case. As $-f$ is increased further, the growth rate drops rapidly and becomes negligible for $-f > 0.4$. The undulations in the f-dependence of the growth rate are accompanied by distinct changes in the spatial structure of the mode, which is braid-centred at $f = 0$ but becomes core-centred above

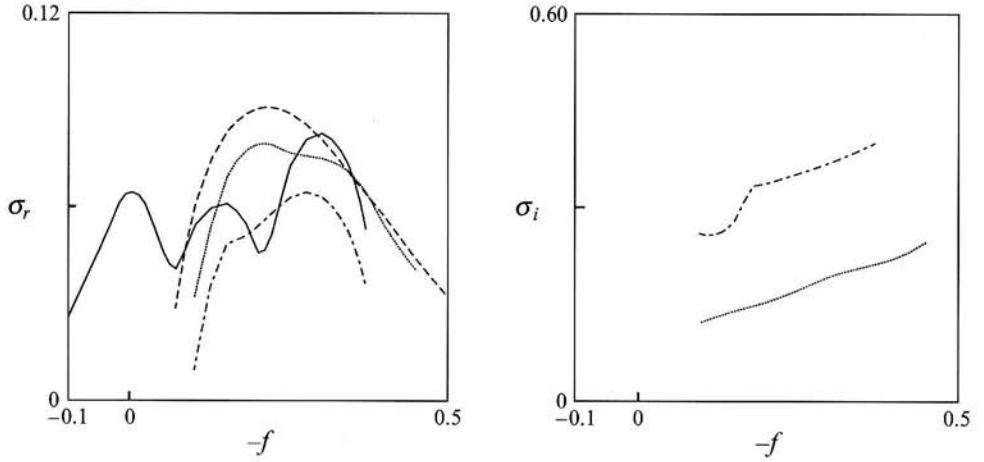

FIGURE 11. Real and imaginary parts of the growth rates of the four most unstable modes and functions of f for $d = 1$. ——, L_1 modes; – – –, edge mode; ..., first harmonic; —·—, second harmonic.

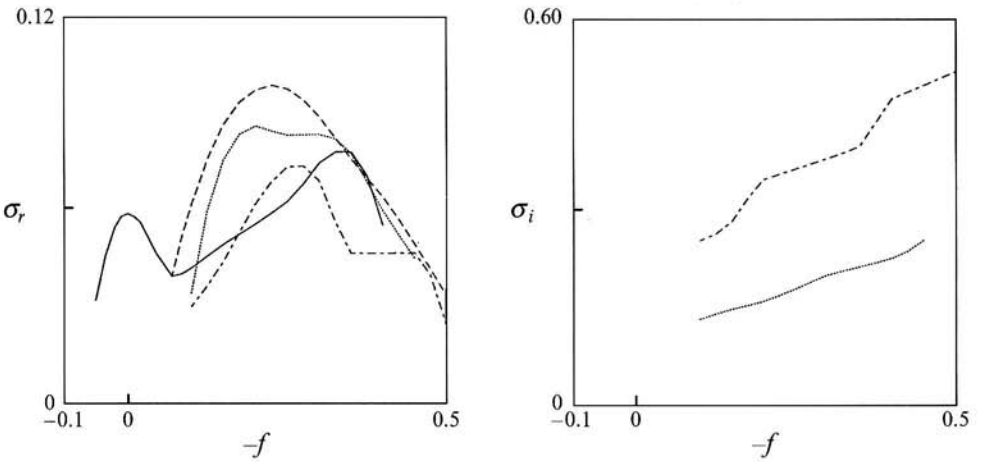

FIGURE 12. Same as figure 11, except that $d = 2$.

$-f = 0.1$ (cf. figure 15). We shall give this mode the designation L_1, as it clearly represents the continuation to non-zero f of the mode which we denoted L_1 in our previous discussion of the non-rotating case.

The dashed curve in figure 11 corresponds to a new mode of instability which we shall refer to as the *edge mode*, since its energy is concentrated in the outer region of the vortex (cf. figure 16). The edge mode achieves a maximum growth rate of 0.0908 at $-f = 0.22$ and is too weak to be resolved for $-f > 0.6$. The dotted and dash-dotted curves in figure 11 indicate the growth rates of the first and second harmonics of the edge mode, respectively. These modes are weaker than the stationary edge mode, but have large enough growth rates that they may be expected to exert a significant influence on the evolution of the flow. Since $d = 1$, the oscillation frequencies are equal to the spanwise phase speeds of the modes, which increase with increasing $-f$ and are on the order of one-tenth of the velocity shift across the original shear layer. These oscillatory modes occur in complex conjugate pairs, and are therefore expected to appear as standing oscillations.

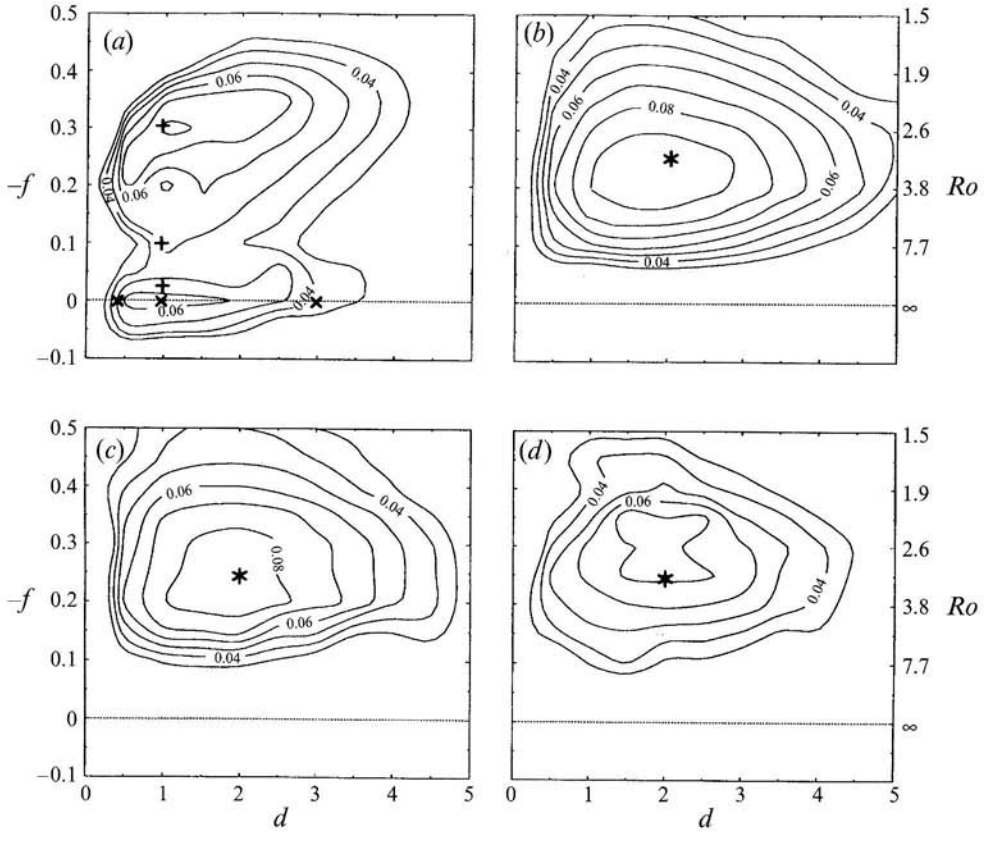

FIGURE 13. Real part of the growth rate as a function of d and f for (a) the L_1 mode, (b) the edge mode and (c, d) the first and second harmonics of the edge mode. Plus signs, crosses and asterisks identify modes whose spatial structures are illustrated in figures 14, 15 and 16, respectively.

In figure 12, we display $\sigma(f)$ curves for the L_1 mode, the edge mode and the harmonics of the latter, calculated at spanwise wavenumber $d = 2$. Qualitatively, the results are similar to those obtained for $d = 1$. Once again, we find that the flow is stabilized for all positive values of f and also for sufficiently small negative f. The edge mode appears at about $-f = 0.07$ and attains its maximum growth rate $\sigma = 0.0979$ at $-f = 0.25$. This is the largest growth rate that we have found in our explorations of the (f, d)-plane, and represents an increase of 60% over the maximum growth rate obtained in the non-rotating case.

Lesieur *et al.* (1991) have performed fully three-dimensional numerical simulations of rotating shear layers, and have found that longitudinal instability is maximized when the Rossby number, measured using the initial maximum relative vorticity, is 5 ± 2. The error tolerance is our estimate, based on Lesieur *et al.* figure 3(b). The equivalent value of $-f$ is between 0.14 and 0.33. Our predicted value $|f_{max}| = 0.25$ is consistent with this result. The equivalent Rossby number for maximum instability, based on the current maximum relative vorticity, is 3.3.

In figure 13, we present contour diagrams of σ_r as a function of spanwise wavenumber and rotation rate for each of the four modes discussed above. The right-hand axes are labelled with the Rossby number. In each figure, the outer contour represents $\sigma_r = 0.03$ while successive contours correspond to $\sigma_r = 0.04, 0.05, \ldots$, etc.

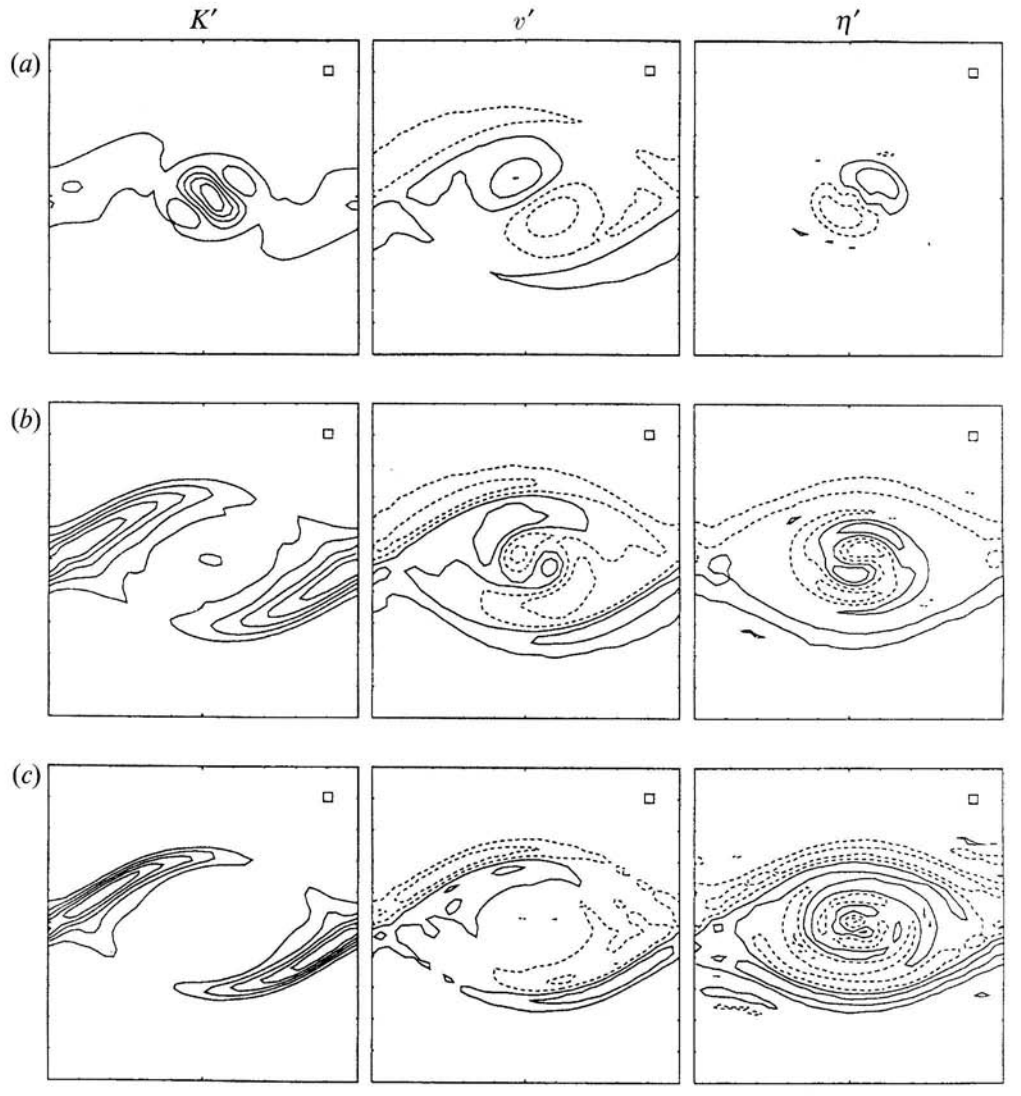

FIGURE 14. Perturbation kinetic energy K', spanwise velocity v' and spanwise vorticity η' fields for the dominant unstable modes at $f = 0$ and (*a*) $d = 0.4$, (*b*) $d = 1$ and (*c*) $d = 3$.

Values below 0.03 are difficult to distinguish reliably in the numerical results and the corresponding contours are therefore omitted. The plus signs, crosses and asterisks which appear on figure 13 represent points at which the spatial structures of the eigenmodes are to be displayed in subsequent figures. For $|f| < 0.07$, the spectrum is dominated by the L_1 mode which occurs in the non-rotating case (figure 13*a*). As was noted in the previous section, the most unstable mode for $f = 0$ is found at $d = 1$. The flow is stable to three-dimensional perturbations for $f > 0.1$ and $f < -0.6$. The latter value corresponds to a Rossby number which is slightly in excess of unity, as would be expected based on the heuristic considerations introduced at the beginning of this section. For $-f > 0.07$, the most unstable mode is the fundamental edge mode whose growth rate is shown in figure 13(*b*). The spanwise wavenumber of the most-unstable mode is close to $d = 2$ for $0.07 < -f < 0.30$ and decreases slightly at larger rotation rates.

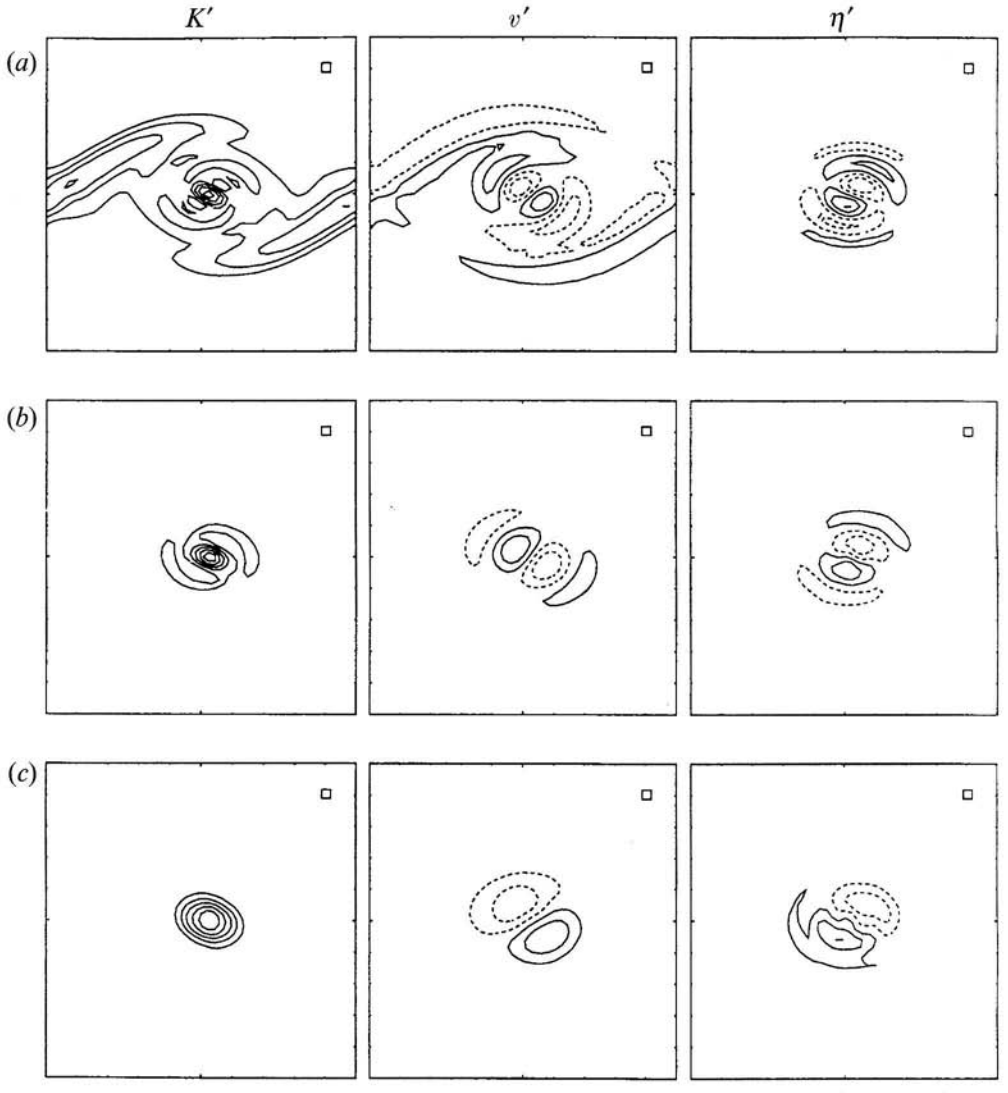

FIGURE 15. Same as figure 14, except that $d = 1$ and (*a*) $-f = 0.02$, (*b*) $-f = 0.1$ and (*c*) $-f = 0.3$.

To facilitate comparison with experimental and numerical results, we note that the spanwise wavelength corresponding to $d = 2$ ($d = 1$) is about one-tenth (one-fifth) of the spacing between the cores of the large vortices. The half-radius of the large vortex is roughly 4 in our units, and the spanwise wavelength corresponding to $d = 2$ ($d = 1$) is about 0.8 (1.6) times this length.

In figures 14, 15 and 16, we display the spatial structures of several of the unstable modes whose growth rates are shown in figure 11. Figure 14 contains the perturbation kinetic energy, spanwise velocity and spanwise vorticity for the dominant modes at $f = 0$, $d = 0.4$, 1.0 and 3.0 (cf. crosses on figure 13*a*). The mode shown in figure 14(*b*) is the most unstable mode for the non-rotating case in the post-pairing phase. The shift from core-centred to braid-centred structure as the spanwise wavenumber is increased is evident upon comparison of figures 14(*a*), 14(*b*) and 14(*c*), particularly if one inspects the v' and η' fields.

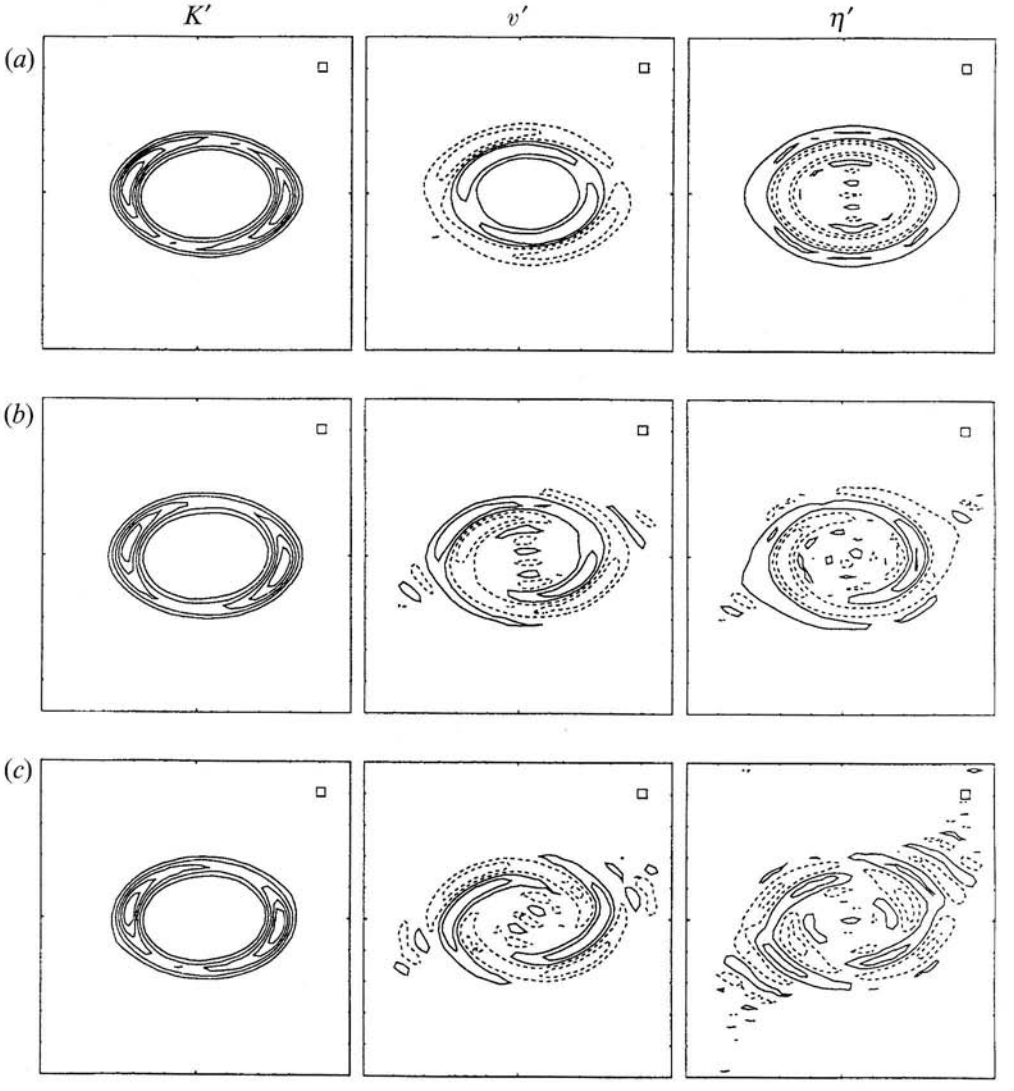

FIGURE 16. Perturbation kinetic energy K', spanwise velocity v' and spanwise vorticity η' fields for (*a*) the fundamental, (*b*) the first harmonic and (*c*) the second harmonic of the edge mode at $-f = 0.25$, $d = 2$.

In figure 15, we illustrate the effect of negative f, by fixing d to unity and displaying the dominant modes for the cases $-f = 0.02$, 0.1 and 0.3 (cf. plus signs on figure 13*a*). Comparison of figures 14(*b*) and 15(*a*) shows that the braid region is stabilized by the inclusion of even a very slow ambient rotation ($f = -0.02$), while the core region is simultaneously destabilized. As $-f$ is increased further, the instability becomes entirely core-centred, as is illustrated in figures 15(*b*) and 15(*c*).

In figure 16, we display the edge mode which occurs at $f = -0.25$, $d = 2$, along with its first and second harmonics (cf. asterisks on figures 13(*b*), 13(*c*) and 13(*d*)). The energy associated with this class of modes is restricted to a very well-defined ring around the edge of the vortex, a morphology which is entirely distinct from that exhibited by the core-centred and braid-centred instabilities. Note that the fundamental edge mode has azimuthal wavenumber 2, while the core modes seen previously exhibit

azimuthal wavenumber 1. This wavenumber is 1 for the first harmonic, 2 again for the second harmonic. The spiral structure of the spanwise velocity fields associated with the harmonics indicates that these modes have the form of helical vortex tubes which propagate along the outside of the vortex in barber-pole fashion as they grow. Numerical simulations of rotating turbulence starting from two-dimensional initial conditions with $R_0 \sim 0.5$ have delivered vortices which exhibit this behaviour (P. Bartello, private communication). Similar structures have also appeared in stability analyses of axisymmetric vortices in a quasi-geostrophic model (Gent & McWilliams 1986).

5. On the mechanisms of three-dimensional instability

The linearized field equations (3) are easily manipulated to form the perturbation enstrophy equation

$$\begin{aligned} Z_t + \tilde{U}Z_x + \tilde{W}Z_z = {} & \tilde{U}_x\xi^2 + \tilde{U}_z\xi\zeta + \tilde{\eta}_a\xi u_y \\ & - \tilde{\eta}_x\eta u - \tilde{\eta}_z\eta w + \tilde{\eta}_a\eta v_y \\ & + \tilde{W}_z\zeta^2 + \tilde{W}_x\xi\zeta + \tilde{\eta}_a\zeta w_y \\ & + Re^{-1}(\xi\nabla^2\xi + \eta\nabla^2\eta + \zeta\nabla^2\zeta), \end{aligned} \tag{17}$$

in which $(\tilde{U}, 0, \tilde{W})$ is the background flow and $(0, \tilde{\eta}, 0)$ is the associated relative vorticity field. (u, v, w) and $(\xi, \eta, \zeta) = (w_y - v_z, u_z - w_x, v_x - u_y)$ are the perturbation velocity and vorticity fields, respectively. $\tilde{\eta}_a$ represents the absolute vorticity $\tilde{\eta} + f$ and $Z = \frac{1}{2}(\xi^2 + \eta^2 + \zeta^2)$ is the perturbation enstrophy. Subscripts denote partial derivatives. Note that we have dropped the primes which were employed in §3 to identify perturbation quantities. The terms on the right-hand side of (17) have been arranged into four groups, each of which appears on a separate line. On the first line, we have terms which govern the evolution of $\frac{1}{2}\xi^2$, the portion of Z which is associated with the streamwise vorticity perturbation. In order of appearance, these three terms represent stretching of ξ by the background velocity field $\tilde{U}$, tilting of ζ by $\tilde{U}$ to create ξ, and tilting of $\tilde{\eta}_a$ by u to produce ξ. Terms on the second line govern the evolution of $\frac{1}{2}\eta^2$. The first two terms on that line (terms 4 and 5) represent the advection of $\tilde{\eta}$ by the perturbation velocity field, while the third (term 6) describes stretching of $\tilde{\eta}_a$ by v. Terms on the third line govern the evolution of $\frac{1}{2}\zeta^2$. In order of appearance, they represent stretching of ζ by the background velocity field $\tilde{W}$, tilting of ξ by $\tilde{W}$ to produce ζ and tilting of $\tilde{\eta}_a$ by w. Terms appearing on the fourth line describe the effects of viscosity.

Our purpose in this section is to assess the relative importance of each of the terms on the right-hand side of (17) in driving the growth of the various classes of unstable modes discussed in §§3 and 4, with a view to obtaining insight into the physical processes which generate instability. Naively, one might hope to identify a single term which is primarily responsible for growth. In that case, a physical explanation for instability would follow easily. We will see, however, that instability can only be driven by a combination of effects, and the physical mechanisms involved must be correspondingly more complex. This result has been suggested previously by Orszag & Patera (1983). Those authors grouped the terms in the perturbation vorticity equation into two sets, and showed that neither set of terms, acting alone, could lead to exponential growth.

For example, one may readily understand how the second and ninth terms of the right-hand side of (17) might combine to generate instability. The process is illustrated

in schematic form in figure 17(*a*). We assume initially that there exists a background spanwise vorticity field $\tilde{\eta}$ and a perturbation streamwise vorticity field ξ. Owing to the action of term nine on the right-hand side of (17), the shear w_y (which is associated with ξ) causes background vorticity filaments to be tilted towards the meridional direction, thereby generating a perturbation meridional vorticity field ζ. In addition, owing to the second term on the right-hand side of (17), the shear $\tilde{U}_z$ (which is associated with $\tilde{\eta}$) tilts ζ filaments towards the streamwise direction. The perturbation streamwise vorticity (ξ) which is created via this second tilting process has the same sign as the ξ field which we postulated originally, and the latter is therefore reinforced. We expect that the positive feedback which is inherent in this two-part process will lead to exponential growth of both ξ and ζ. The perturbation vorticity vector that is reinforced by this interaction lies in the (x,z)-plane and points up and to the right (or, in geophysical terms, to the northeast). Had we postulated a ξ field with the opposite sign to that shown in figure 17(*a*), the preferred perturbation vorticity would point down and to the left (i.e. to the southwest). Because the background flow is independent of y, the direction of the perturbation vorticity alternates sinusoidally between these two orientations as one moves in the y-direction.

The pair of terms just mentioned contains one member which describes an action exerted by the background flow on the perturbation and one which describes the action of the perturbation on the background flow. This characteristic is necessary if the pair of terms is to involve a feedback loop. The aforementioned grouping of terms which was employed by Orszag & Patera (1983) was, in fact, a division of the terms on the right-hand side of the vorticity equation into those describing the action of the background flow on the perturbation ('action' meaning advection, stretching or tilting) and those which describe the action of the perturbation on the background flow (also see Bayly *et al.* 1988). In (17), the corresponding division would place terms 1, 2, 7 and 8 plus the advection terms on the left-hand side into the first category, and terms 3, 4, 5, 6 and 9 into the second. From this perspective, it is easy to understand why Orszag & Patera found that neither set of terms, acting alone, could generate exponential growth: positive feedback can occur only if terms from both categories are active.

Combinations of tilting terms may also interact destructively. In figure 17(*b*), we again postulate a local ξ field and consider the ζ field which would result from the tilting action of ξ on $\tilde{\eta}_a$ (term 9). However, we now consider the tilting action of ζ on $\tilde{\eta}_a$ via term three on the right-hand side of (17). This action creates an additional streamwise vorticity perturbation whose sign is opposite to that of the initial ξ field. These two effects therefore act in competition with one another.

Note that each vorticity component represents the sum of two spatial velocity derivatives, e.g. $\tilde{\eta} = \tilde{U}_z - \tilde{W}_x$. In the foregoing examples we have implicitly assumed that each term in each such sum has the same sign, and therefore has the same sign as the vorticity component. In figure 17(*c*) we illustrate a case in which this is not true, since $\tilde{U}_z > 0$ and $-\tilde{W}_z < 0$. This situation occurs in the strained regions (braids) which separate the large vortices. In this instance, terms 2 and 8 on the right-hand side of (17) interact constructively. The reverse situation, in which $\tilde{U}_z$ and $-\tilde{W}_x$ have the same sign, occurs in the vortex cores. In that case, terms 2 and 8 compete. (An assumption similar to that described above has been made with respect to the perturbation vorticity field. Specifically, we have assumed that the factors u_y and w_y, which appear in terms 3 and 9 on the right-hand side of (17), may be treated as qualitatively equivalent to the vorticity components $-\zeta$ and ξ, respectively. This assumption may be justified on the grounds that adjacent secondary vortices are automatically counter-rotating, owing to

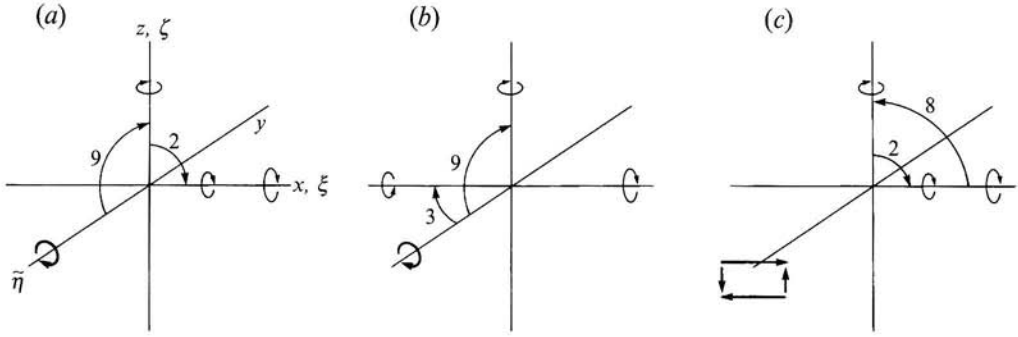

FIGURE 17. (*a*) Mechanism of positive feedback between terms 9 and 2 on the right-hand side of (17). (*b*) Destructive interference between terms 9 and 3. (*c*) Positive feedback between terms 2 and 8 in a strained region.

periodicity in y, and are therefore separated by regions of pure translation rather than by regions of strain.)

Figure 17 illustrates only a few of the many possible interactions between vortex tilting mechanisms (i.e. between the processes described by terms 2, 3, 8 and 9 on the right-hand side of (17)). Clearly, an unstable normal mode must be spatially configured so as to take maximal advantage of some interaction which promotes growth, while avoiding effects which retard that process. The stretching effects represented by terms 1 and 7 may further reinforce the ξ and ζ fields, but those effects, acting alone, cannot drive exponential growth since they involve no positive feedback.

We have now seen how the physical processes described by the terms on lines one and three of the right-hand side of (17) may interact to govern the evolution of the enstrophy associated with the ξ and ζ fields. The terms on the second line, which affect only the perturbation spanwise vorticity, will be shown later in this section to be relatively unimportant. Terms 4 and 5 may drive growth via downgradient transfer of background vorticity, a process which is similar to the generation of two-dimensional instability in parallel flow via downgradient momentum transport (e.g. Smyth & Peltier 1989). Term 6 represents the stretching of background vorticity by the spanwise velocity perturbation, as was discussed in the previous section. The remaining terms (those appearing on line four) describe viscous effects, and act only to damp instability.

To cast (17) into a form which is more useful for the present purpose, we apply the spatial averaging operator

$$\langle \cdot \rangle = \int_0^{2\pi/\alpha} \mathrm{d}x \int_0^{2\pi/d} \mathrm{d}y \int_0^H \mathrm{d}z,$$

which removes the spatial dependences, annihilates the second and third terms on the left-hand side of (17) and renders the viscous terms negative semidefinite. (Note that this definition of the averaging operator differs slightly from that employed in previous sections.) We then assume that the perturbation consists of a single unstable mode, so that $\langle Z_t \rangle$ may be replaced by $2\sigma\langle Z \rangle$, and finally divide through by $2\langle Z \rangle$. The resulting equation reveals the portion of the growth rate which is contributed by each of the terms on the right-hand side of (17), namely:

$$\sigma = \sum_{k=1}^{10} \sigma_k, \tag{18}$$

(f,d)	(0.3, 1.0)	(0, 1.0)	(0.25, 2.0)	(0, 3.0)	(0, 0.4)
Type	Core	Braid	Edge	Braid	Core
$Z^{(x)}$	0.439	0.491	0.580	0.498	0.445
$Z^{(y)}$	0.170	0.077	0.129	0.011	0.290
$Z^{(z)}$	0.390	0.432	0.291	0.492	0.264
σ	0.0827	0.0642	0.0979	0.0428	0.0589
σ_1	0.0002	0.0145	0.0345	0.0158	0.0082
σ_2	0.1773	0.0463	0.0292	0.0478	0.0670
σ_3	−0.1383	−0.0263	0.0032	−0.0262	−0.0474
σ_4	−0.0054	0.0016	0.0028	0.0001	−0.0012
σ_5	0.0127	0.0018	0.0053	0.0000	0.0106
σ_6	0.0074	0.0025	0.0074	0.0008	0.0091
σ_7	0.0011	−0.0093	0.0179	−0.0100	−0.0053
σ_8	−0.0969	0.0125	0.0282	0.0212	−0.0184
σ_9	0.1286	0.0268	−0.0131	0.0255	0.0400
σ_{10}	−0.0078	−0.0062	−0.0194	−0.0323	−0.0037

TABLE 1. Partial enstrophies, total and partial growth rates [cf. (17), (18)] for five of the unstable modes discussed in §4

in which $\sigma_k = s_k/2\langle Z\rangle$ and

$$s_1 = \langle \tilde{U}_x|\hat{\xi}|^2\rangle \qquad s_2 = \langle \tilde{U}_z(\hat{\xi}\hat{\zeta}^*)_i\rangle \qquad s_3 = d\langle \tilde{\eta}_a(\hat{\xi}\hat{u}^*)_i\rangle$$
$$s_4 = -\langle \tilde{\eta}_x(\hat{u}\hat{\eta}^*)_r\rangle \qquad s_5 = -\langle \tilde{\eta}_z(\hat{w}\hat{\eta}^*)_r\rangle \qquad s_6 = d\langle \tilde{\eta}_a(\hat{\eta}\hat{v}^*)_i\rangle$$
$$s_7 = \langle \tilde{W}_z|\hat{\zeta}|^2\rangle \qquad s_8 = \langle \tilde{W}_x(\hat{\xi}\hat{\zeta}^*)_i\rangle \qquad s_9 = d\langle \tilde{\eta}_a(\hat{\zeta}\hat{w}^*)_i\rangle$$
$$s_{19} = -Re^{-1}\langle(|\nabla\hat{\xi}|^2+|\nabla\hat{\eta}|^2+|\nabla\hat{\zeta}|^2)\rangle.$$

The subscripts r and i denote the real and imaginary parts, respectively, and stars indicate complex conjugation. $(\hat{u},\hat{v},\hat{w})$ and $(\hat{\xi},\hat{\eta},\hat{\zeta})$ are the complex amplitudes of the perturbation eigenfunctions. The reader will note that the three viscous terms which appear on the right-hand side of (17) have been combined into a single expression s_{10}. Otherwise, the ordering of the terms on the right-hand side of (17) has been preserved.

In table 1, we display the total growth rate σ and the partial growth rates σ_k for a representative subset of the unstable modes which were discussed in §4. Also included in table 1 are the values of the fractional enstrophies $Z^{(x)} = \langle\frac{1}{2}\xi^2\rangle/\langle Z\rangle$, $Z^{(y)} = \langle\frac{1}{2}\eta^2\rangle/\langle Z\rangle$, and $Z^{(z)} = \langle\frac{1}{2}\zeta^2\rangle/\langle Z\rangle$. These quantities indicate the overall orientation of the perturbation vorticity field. Note that ξ is generally the strongest component of the perturbation vorticity, while η is generally the weakest. As was done in the previous section, we group the unstable modes into three categories based on the spatial location at which the perturbation is strongest, i.e. core modes, braid modes and edge modes. In the following three subsections, we shall discuss the physical mechanism that supports the growth of each of these classes of modes in turn.

5.1. *The core mode*

In this subsection, we shall consider the core-centred mode which dominates the spectrum at $f = 0.3$, $d = 1$ (cf. figure 15*c*). Core modes are found in many regions of the (f,d)-plane (figure 13*a*); their properties are qualitatively similar and are well represented by this example. Referring to the data given in the first column of table 1, we see that the perturbation enstrophy is dominated by the terms $\frac{1}{2}\xi^2$ and $\frac{1}{2}\zeta^2$, so that the perturbation vorticity tends to be oriented close to the (x,z)-plane. In addition, the

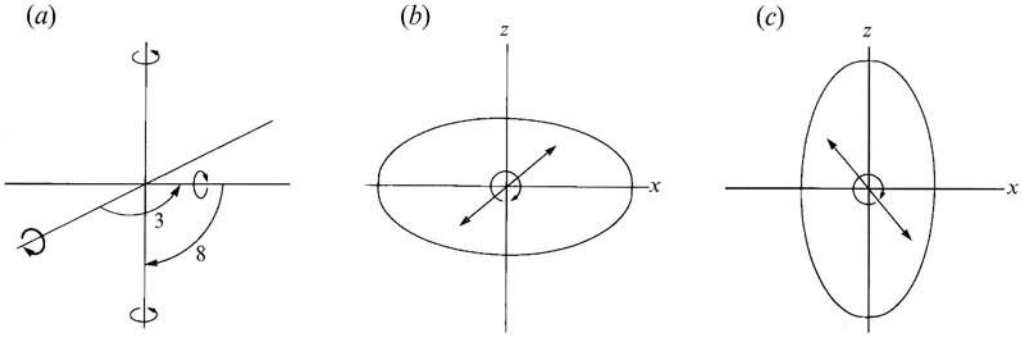

FIGURE 18. (*a*) Mechanism of positive feedback between terms 3 and 8 on the right-hand side of (17). (*b*) Clockwise vortex whose aspect ratio exceeds unity. The two-ended arrow indicates the preferred orientation of the perturbation vorticity. (*c*) Same as (*b*) but with aspect ratio less than unity. If the sense of the background vorticity is counterclockwise, the orientations of the perturbation vorticity vectors in (*b*) and (*c*) are interchanged.

partial growth rates σ_4, σ_5 and σ_6, which correspond to the terms on the right-hand side of (17) that govern the evolution of $\frac{1}{2}\eta^2$, are relatively small. Spanwise perturbation vorticity is therefore of secondary importance for this mode.

Turning to the terms which govern the evolution of $\frac{1}{2}\xi^2$ and $\frac{1}{2}\zeta^2$, namely terms 1, 2 and 3 and terms 7, 8 and 9, we see that the contributions of largest magnitude come from the tilting terms 2, 3, 8 and 9. It is not surprising that the stretching terms (terms 1 and 7) are unimportant in this example, since the $\tilde{U}_x$ and $\tilde{W}_z$ fields, to which those terms are proportional, are very weak in the core region.

Terms 2 and 8 describe the tilting of perturbation vorticity filaments by the background flow, while terms 3 and 9 represent tilting of the background absolute vorticity $\tilde{\eta}_a$ by the perturbations. As was noted in the previous subsection, a pair of terms which delivers positive feedback (and consequently exponential growth) must contain one term of each type. In the discussion of figure 17(*a*), we saw how terms 9 and 2 interact to form a feedback loop. (For brevity, we shall subsequently refer to this mechanism as the '9–2 loop'.) The perturbation vorticity field which is reinforced by this loop points upwards and to the right (or the reverse). In figure 18(*a*), we illustrate a similar interaction between terms 3 and 8. A given vertical vorticity perturbation ζ tilts the background vorticity $\tilde{\eta}_a$ to create ξ (term 3), while the resulting ξ is tilted by the background vorticity (term 7) to reinforce the ζ perturbation which we postulated originally. We call this mechanism the '3–8 loop', and note that it acts to reinforce a perturbation vorticity which points downwards and to the right (or the reverse). The reader will note that the 3–8 loop and the 9–2 loop are identical but for a 90° rotation in the (x, z)-plane.

The tilting terms in (17) therefore support two positive feedback mechanisms, either of which could drive exponential growth. However, these two mechanisms act in opposition to one another. We saw in figure 17(*b*) that terms 3 and 9 work against each other; a similar result holds for terms 2 and 8. Therefore, if the 9–2 loop and the 3–8 loop operate simultaneously and with similar strength, we expect that the resulting destructive interference will prevent instability from occurring. If the 9–2 loop dominates, then we expect to observe an unstable mode for which the vorticity vectors point upwards and to the right, while dominance of the 3–8 loop generates instability such that the perturbation vorticity points downwards and to the right.

Which property of the background flow determines which feedback loop, if either, will dominate? Inspection of (17) shows that terms 3 and 9 are both proportional to

the absolute vorticity $\tilde{\eta}_a$, while term 2 is proportional to $\tilde{U}_z$ and term 8 is proportional to $\tilde{W}_x$. Note also that the factor $\xi\zeta$ is common to the latter two terms. While there is nothing to choose, *a priori*, between terms 3 and 9, the relative magnitudes of terms 2 and 8 are clearly governed by the relative magnitudes of $\tilde{U}_z$ and $\tilde{W}_x$. The relative magnitudes of the latter two fields are determined by the ellipticity of the vortex core. If the core is elliptical with aspect ratio exceeding unity then $|\tilde{U}_z| > |\tilde{W}_x|$. As a result, the 9–2 loop dominates and the vorticity perturbation points upwards and to the right, as is illustrated in figure 18(*b*). On the other hand, if the aspect ratio is less than unity, then $|\tilde{W}_z| > |\tilde{U}_x|$ and the 3–8 loop dominates, as shown in figure 18(*c*). Note that the orientations of the preferred vorticity perturbations in the two cases shown in figures 18(*b*) and 18(*c*) would be interchanged if the background vorticity were counter-clockwise rather than clockwise. The foregoing observations may be summarized concisely by stating that the preferred vorticity perturbation on an elliptical vortex is oriented in the quadrant located downstream of the semi-minor axis. Finally, if the ellipticity of the vortex core vanishes, the two feedback mechanisms cancel and there is no instability. This property is obviously reminiscent of the elliptical instability, which was shown in §3.1 to represent a reasonable idealization of the core modes which our stability analyses have delivered.

In the present instance, the aspect ratio of the vortex core exceeds unity, and we therefore expect that the 9–2 feedback loop will dominate. Inspection of the data given in table 1 confirms that growth of the core mode is driven primarily by terms 9 and 2 and is opposed by terms 3 and 8. Closer inspection of the results of the stability analyses also reveals that the perturbation vorticity field tends to point up and to the right or down and to the left, as expected. For example, we show in figure 19 selected filaments of the total vorticity field, i.e. $\tilde{\eta}$ plus a perturbation proportional to the core mode, and note that the orientation of the filaments is consistent with the scenario illustrated in figure 18(*b*). From careful comparison of Pierrehumbert's (1986) figure 2 and our figure 3 (or any of our figures 14(*a*), 15(*b*) and 15(*c*), it may be inferred that the idealized elliptical instability exhibits the same spatial structure (i.e. that shown in figure 18*b*). This orientation of the perturbation vorticity field is also visible in the linear numerical simulations of Corcos & Lin (1984, figure 13).

Detailed investigations of core-centred modes which occur in other regions of the (f, d)-plane (figure 13*a*) have yielded results similar to those described above. To illustrate this, we present data pertaining to a second example of a core mode, namely that found at $f = 0$, $d = 0.4$ (figure 14*a*) in the fifth column of table 1. Comparing columns 5 and 1, we see that the relative magnitudes of the σ_k are qualitatively similar in the two cases. These results further reinforce our conviction that the instability mechanism described above is valid for core-centred modes in general. We conclude that the core modes discovered here may be identified with Pierrehumbert's (1986) elliptical instability, and that this instability is driven primarily by a feedback loop in which ξ tilts $\tilde{\eta}_a$ to create ζ, and $\tilde{\eta}_a$ simultaneously tilts ζ to reinforce ξ. The result is an instability which can only occur when the vortex core exhibits non-zero ellipticity, and which has the spatial structure that is represented schematically in figure 18(*b*).

5.2. *The braid mode*

We turn now to an examination of the mechanics of the braid mode, using as an example the unstable mode found at $f = 0$, $d = 1$ (cf. figure 14*b*). The relevant results are shown in the second column of table 1. For purposes of comparison, the corresponding data for a second example of a braid mode are shown in the fourth column. As in the case of the core mode, we observe that the perturbation vorticity

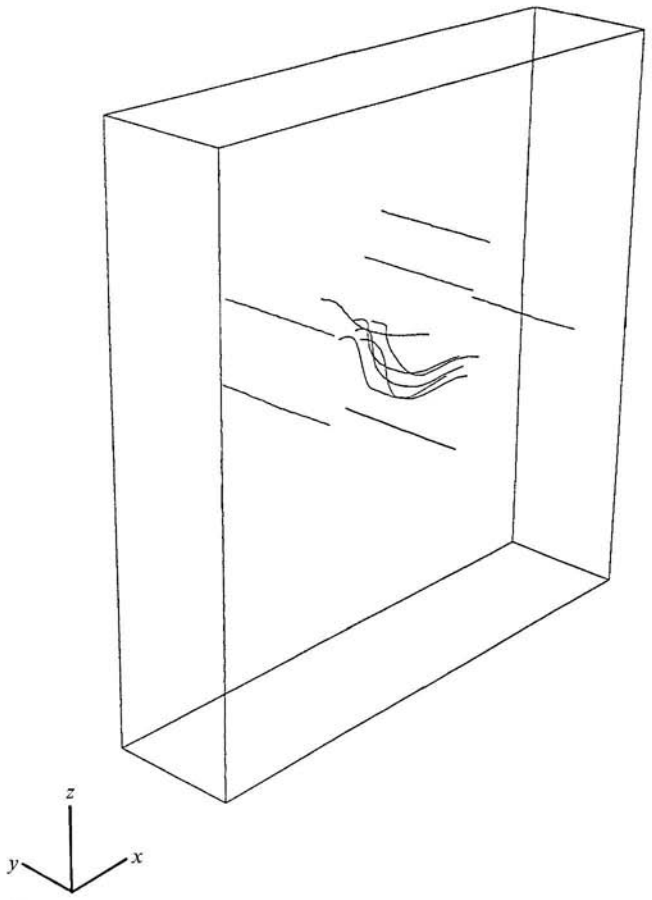

FIGURE 19. Selected vortex filaments for the vorticity field consisting of the background vortex plus a perturbation proportional to the core mode.

vector tends to lie close to the (x, z)-plane, and that the partial growth rates σ_3, σ_4 and σ_6, which contribute to the growth of the spanwise vorticity, are correspondingly small.

In contrast to the previous case, we find that the stretching terms (1 and 7) are comparable in magnitude to the tilting terms (2, 3, 8 and 9). Detailed examination of the spatial dependences of these terms reveals that the stretching terms act only near the tips of the perturbation vortex tubes (cf. figure 14*b*), while the tilting terms are active throughout the spatial extent of the eigenmode. In particular, the tilting terms are solely responsible for the growth of the perturbation in the region near the stagnation point. (This is because the $\tilde{U}_x$ and $\tilde{W}_z$ fields, to which the stretching terms are proportional, are weak in this region.) From the morphology of the background flow, it is clear that perturbation enstrophy is created in the stagnation region by the tilting terms, and is subsequently advected along the principal axis of strain to a region on the edge of the large vortex in which $|\tilde{U}_x|$ and $|\tilde{W}_z|$ are large, and the stretching terms can therefore modify the perturbation. The fact that the stretching terms act in opposition to each other (i.e. $\sigma_1 \sigma_7 < 0$) is a simple consequence of incompressibility.

As in the case of the core mode, we find that the growth of the braid mode in the stagnation region is driven primarily by the 9–2 feedback loop. In contrast to the previous case, however, growth is now aided by term 8, and opposed only by term 3. This is because, although the background vorticity $\tilde{\eta} = \tilde{U}_z - \tilde{W}_x$ is positive in the

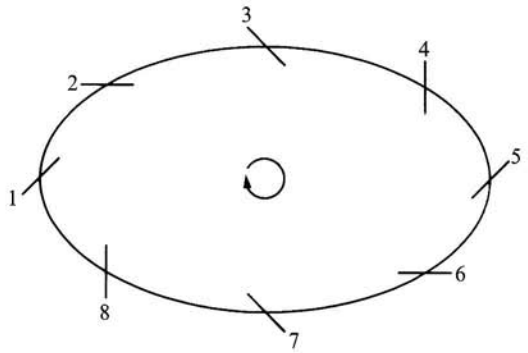

FIGURE 20. The approximate orientation of the perturbation vorticity associated with the edge mode at selected points on the edge of the background vortex.

strained region (as it is everywhere), $\tilde{U}_z$ and $-\tilde{W}_x$ have opposite signs. Referring to figures 17(*a*) and (17(*c*), we see that term 8 now acts in concert with terms 2 and 9, creating a three-way feedback loop. Term 3, however, acts in opposition to this mechanism, as is shown in figure 17(*b*).

We conclude that the enstrophy associated with the braid mode is created near the stagnation point by a positive feedback loop involving the tilting of $\tilde{\eta}$ by ξ to create ζ, the tilting of ζ by $\tilde{U}_z$ to create ξ and the tilting of ξ by $\tilde{W}_x$ to create ζ. The tilting of $\tilde{\eta}$ by ζ opposes this process by creating ξ of the wrong sign. Enstrophy generated via this process is advected away from the stagnation region and is subsequently enhanced by the total effect of the stretching terms. The scenario just described is consistent with that proposed by Corcos & Lin (1984); its validity is confirmed in the present study via the quantitative analysis of the perturbation enstrophy budget.

5.3. *The edge mode*

The physical mechanism of the edge mode (figure 16*a*) is more complex than that of either the core mode or the braid mode, since the morphology of the background flow in the edge region is more complicated than either the simple rotation of the core or the strain field found in the braid regions. Nevertheless, the understanding of the core and braid modes which we have developed in the previous two subsections equips us well to understand the more intricate mechanism of the edge mode.

Examining the third column of table 1, we see that the perturbation vorticity is, as usual, mainly confined to the (x, z)-plane. It is evident that a relatively large number of terms contribute to the growth of the modes. Overall, terms 1, 2, 7 and 8 act to promote growth, while term 9 acts in opposition. However, close inspection of the spatial dependences of the quantities appearing on the right-hand side of (17) reveals that different terms are important at different spatial locations. In particular, terms 3 and 9 are large and positive in some regions, large and negative in others, so that the spatially averaged magnitudes of those terms presented in table 1 are misleading. The advection terms which appear on the left-hand side of (17) do not affect the spatially-averaged perturbation enstrophy, but they dominate locally, acting to carry the perturbation in the clockwise direction around the edge of the vortex.

The approximate orientation of the perturbation vorticity vector as a function of space is shown in figure 20. Eight stations on the edge of the vortex have been marked for reference in the discussion which follows. At station 1, the eigenvalues of the strain tensor (cf. figure 10*b*) are real, and the flow geometry is therefore essentially that of a strain field. At station 2, the stretching field $\tilde{U}_x$ is large and positive. The dynamics of

the instability in this region are therefore similar to those of the braid mode (cf. §5.2). At station 1, the tilting terms interact to create perturbation vorticity which points up and to the right (or the reverse). That disturbance is advected to station 2, where its x-component is enhanced by the stretching action of term 1.

In the vicinity of station 3, the eigenvalues of the strain tensor are imaginary, and the flow therefore has the character of a rotation. As a result, the mechanism of instability is similar to that found in the core region (cf. §5.1). In addition, $|\tilde{W}_x| > |\tilde{U}_z|$ in this region, so that the 3–8 feedback loop is stronger than the 9–2 loop and the resulting vorticity perturbation points downwards and to the right (or the reverse). Perturbation vorticity created by this mechanism is then advected to station 4, where $\tilde{W}_z$ is large and positive. As a result, the meridional vorticity ζ is enhanced by the stretching action of term 7.

As the disturbance is carried onward past stations 5–8, the sequence of processes described above is repeated. In summary, the edge mode is driven by a combination of the processes which drive the core mode and those which drive the braid mode, aided by the advective action of the background flow.

6. Summary

Our goal in this study has been to gain insight into the manner in which small-amplitude three-dimensional circulations develop in otherwise two-dimensional flow. This three-dimensionalization process is of particular interest in the context of geophysical fluid dynamics, since geophysical flows are often strongly dominated by horizontal motions. We have chosen to focus on a horizontal flow that consists of the array of barotropic vortices which forms as a result of the growth and pairing of Kelvin–Helmholtz waves on a meridionally-sheared zonal current. (The specification of zonal initial flow is made for definiteness only; the validity of our results is independent of the direction of the horizontal flow.) Rotational effects have been incorporated by invoking the f-plane approximation (e.g. Gill 1982).

As our starting point, we have considered the special case in which $f = 0$. In the context of this special case, the competition between three-dimensional instabilities and the transverse pairing mode which dominates the two-dimensional evolution of the flow has been investigated. We have tested the stability of the two-dimensional flow to three-dimensional perturbations during three separate phases of the evolution of the two-dimensional flow, namely the pre-pairing, pairing and post-pairing regimes. To account for the time-dependence of the two-dimensional flow, we have supplemented the standard multiple-timescale method of stability analysis with the newly-developed TASM technique.

In the pre-pairing phase, we have found that the spectrum of secondary instability is dominated at high spanwise wavenumbers ($d > 1.5$) by modes which are configured such that the perturbation kinetic energy is concentrated in the braids between the large vortices, at moderate wavenumbers ($0.3 < d < 1.5$) by motions which are concentrated in the vortex cores, and at low wavenumbers ($d < 0.3$) by the pairing mode. We have found it natural to separate the various instabilities into two groups: those whose streamwise wavelengths are similar to that of the large vortices (the longitudinal modes), and those whose streamwise wavelengths are twice that of the large vortices (the subharmonic modes). The former class of modes includes PW's translative instability as well as the braid mode which was first observed in the laboratory experiments of Breidenthal (1981). The latter category includes the pairing instability, which becomes PW's helical pairing mode at small but non-zero spanwise

wavenumber, as well as a number of smaller-scale helical pairing modes whose existence has not been noted previously. These new modes exhibit strong helicity, and growth rates which render them competitive with the previously discovered instabilities listed above. The subset of modes whose energy is concentrated in the vortex cores have been identified as manifestations of Pierrehumbert's (1986) elliptical instability.

During pairing, the spectrum is dominated by the unstable modes of the emerging subharmonic vortex. Modes which are associated with the original KH vortices are rapidly stabilized once pairing has begun. Since the growth rates of the unstable modes associated with the single (merged) vortex state are roughly half those of the corresponding modes in the pre-pairing state, we observe a marked stabilization of the flow at the onset of pairing. This result concisely explains the results of Metcalfe *et al.*'s (1987) three-dimensional simulations.

Although the core-centred modes exhibit substantial growth rates, the most unstable modes are those whose energy is concentrated in the braid regions. Corcos & Lin (1984) have addressed the problem of three-dimensionalization of an evolving shear layer by solving the linear initial-value problem directly (cf. (7) and the accompanying discussion). In that study, it was concluded that three-dimensional circulations occur primarily in the vortex cores. The reason for the apparent discrepancy with the results reported here lies in Corcos & Lin's choice of values for the spanwise wavenumber. They employed values in the range $0.1 < d < 0.7$, and therefore did not observe the dominance of the braid mode, which occurs at higher values of d. It is also possible that additional calculations performed using larger d would have delivered relatively low growth rates in consequence of the low Reynolds number ($Re = 50$) which Corcos & Lin assumed in their analyses.

It has often been remarked (e.g. PW; Orszag & Patera 1983; Pierrehumbert 1986; Smyth & Peltier 1991) that three-dimensional modes tend to be strongly unstable over a broad range of spanwise wavenumbers whose extent is limited only by viscous effects, i.e. that three-dimensional instability is capable of transferring energy from large-scale motions directly into the viscous subrange. In our investigations of the non-rotating ($f = 0$) case, we have found that the time-dependence of the two-dimensional flow, however weak it may be, can act to decorrelate small-scale modes and therefore to impose a short-wave cutoff on the spectrum independently of the action of diffusion. This has led us to suggest that the direct transfer of energy into the dissipative subrange may occur only when the two-dimensional flow is precisely in equilibrium.

In our analyses of the rotating case, we have focused (without significant loss of generality) upon the post-pairing phase. We have seen that weak anticyclonic rotation (i.e. rotation which tends to bring the absolute vorticity of the mixing layer closer to zero than is the relative vorticity) acts to destabilize the flow. Maximal destabilization is found when $f = -0.25$ (or when the Rossby number $R_0 = \tilde{\eta}_+/f$, in which $\tilde{\eta}_+$ is the current maximum vorticity in the vortex core, takes the value 3.3). In this instance, the growth rate of the most unstable mode is 0.0979 (in units of the original maximum vorticity), compared with 0.0645 in the non-rotating case. The spanwise wavenumber of the most unstable mode is then $d = 2$ (in units of the original half-depth of the shear layer), compared with $d = 1$ in the non-rotating case. Alternatively, the spanwise wavelength is slightly less than the radius (resp. diameter) of the two-dimensional vortex in the rotating (resp. non-rotating) case. The energy of the most unstable mode for the case $f = -0.25$ is concentrated around the edge of the two-dimensional vortex, and we therefore refer to this mode as the edge mode. This new mode of instability is a unique property of rotating flows, in that its structure differs qualitatively from that of any instability which has been found previously in the non-rotating case. In contrast,

the energy of the dominant mode for the non-rotating case is concentrated in the braids between the large vortices. As expected in consequence of Lesieur *et al.* s (1991) numerical simulation results, we have found that rapid anticyclonic rotation, or cyclonic rotation at any speed, acts to stabilize the flow.

In §5, we have sought to present mechanistic explanations for several aspects of the three-dimensionalization process. We have found that the core modes (and hence Pierrehumbert's elliptical instability) are driven by the interaction of two pairs of vortex tilting mechanisms, either of which would generate exponential growth if acting alone, but which act in opposition to each other. The relative strengths of these two mechanisms are determined by the ellipticity of the vortex core; if this ellipticity vanishes then the two mechanisms cancel and there is no instability. Consideration of these two competing growth mechanisms has also enabled us to predict the spatial morphology of the core modes. Similar mechanistic descriptions have been presented for the braid modes, and for the fundamental edge mode which dominates the instability spectrum in the rotating case.

The view that three-dimensional instability of two-dimensional flow is driven primarily by interactions of vortex tilting terms was first enunciated (to our knowledge) by Orszag & Patera (1983). Our goal in §5 has been to describe that scenario in detail and to demonstrate its importance quantitatively via an analysis of the perturbation enstrophy budget. An alternative view, stated most recently by Waleffe (1990), holds that three-dimensional perturbations grow as a result of the stretching of perturbation vorticity by the strain field associated with the two-dimensional flow. Waleffe provides an example of a perturbation that grows exponentially as a result of this mechanism. However, that perturbation is unrealistic in that it is spatially uniform, and therefore obeys no boundary conditions. Orszag & Patera (1983) have proved rigorously that the deformation of perturbation vorticity by the background flow cannot drive normal-mode instability. The results described in the present paper strongly suggest that, while vortex stretching is not unimportant, the three-dimensionalization process is driven primarily by positive feedback between pairs of vortex tilting terms.

We have so far been unable to determine why the presence of non-zero f influences the spatial structure of the preferred instability as it does. Lesieur (1991, §3.3.1) has suggested that the most unstable regions of the two-dimensional background flow should be those in which the deformation is large and in which the absolute vorticity is small. Our observation that the braid mode is dominant when $f = 0$ while the edge mode dominates when $f < 0$ is consistent with this proposal. The braid regions are moderately deformed and have $\tilde{\eta}_a$ close to zero when $f = 0$, whereas the edge region is strongly deformed and has $\tilde{\eta}_a$ close to zero when $f < 0$. The existence of strongly unstable core modes, in both the non-rotating and rotating cases, seems inconsistent with this picture since the core region is rapidly rotating and is only weakly deformed. However, the physical arguments given in §5.1 suggest that this weak deformation is crucial to the growth of the instability. In addition, we have seen that the core region becomes more unstable as $-f$ increases, i.e. as the absolute vorticity is decreased. Our results therefore indicate that either a deformed background flow or a small value of the absolute vorticity (i.e. $|\tilde{\eta} + f| \approx 0$) may be locally conducive to instability, as Lesieur has suggested.

Additional insight into this issue may be obtained by considering the mechanism of inertial instability, via which an axisymmetric vortex exhibits growing, axisymmetric perturbations. Using mechanistic arguments, Rayleigh (1916) showed that this instability should occur wherever the product of the angular velocity $\tilde{\omega}$ and the vorticity $\tilde{\eta}$ of the background flow is negative. The same arguments apply in a rotating

reference frame, provided that the angular velocity and vorticity are evaluated in the inertial frame, i.e. $\tilde{\Omega} \rightarrow \tilde{\Omega}_a = \tilde{\Omega} + \frac{1}{2}f$, $\tilde{\eta} \rightarrow \tilde{\eta}_a = \tilde{\eta} + f$ (Kloosterzeil & van Heijst 1991). In the present case, the spatial location of the edge mode corresponds in a crude sense to the region in which $\tilde{\Omega}_a \tilde{\eta}_a$ is negative. In the cyclonic case, $\tilde{\Omega}_a \tilde{\eta}_a$ is positive definite, and the edge instability does not occur. Although Rayleigh's assumption of axisymmetric flow is violated in the present case, it seems plausible that the physical mechanism could be similar, i.e. that the edge mode could be essentially a manifestation of inertial instability.

REFERENCES

BARTELLO, P., MÉTAIS, M. & LESIEUR, M. 1994 Coherent structures in rotating three-dimensional turbulence. *J. Fluid Mech.* (submitted).

BAYLY, B. J. 1986 Three-dimensional instability of elliptical flow. *Phys. Rev. Lett.* **57**, 2160–2163.

BAYLY, B. J., ORSZAG, S. A. & HERBERT, T. 1988 Instability mechanisms in shear-flow transition. *Ann. Rev. Fluid Mech.* **20**, 359–391.

BENZI, R., PATARNELLO, S. & SANTANGELO, P. 1988 Self-similar coherent structures in two-dimensional decaying turbulence. *J. Phys.* A: *Math. Gen.* **21**, 1221–1237.

BERNAL, L. P. & ROSHKO, A. 1986 Streamwise vortex structure in plane mixing layers. *J. Fluid Mech.* **170**, 499–522.

BREIDENTHAL, R. E. 1981 Structure in turbulent mixing layers and wakes using a chemical reaction. *J. Fluid Mech.* **109**, 1–24.

BROWAND, F. K. & HO, C. M. 1983 The mixing layer: an example of quasi two-dimensional turbulence. *J. Mec. Num. Spec.* 99–120.

BROWN, G. L. & ROSHKO, A. 1974 On density effects and large-scale structure in turbulent mixing layers. *J. Fluid Mech.* **64**, 775–816.

COMTE, P., LESIEUR, M. & LAMBALLAIS, E. 1992 Large and small-scale stirring of vorticity and a passive scalar in a 3D temporal mixing layer. *Phys. Fluids* A **4**, 2761–2778.

CORCOS, G. M. & LIN, S. J. 1984 The mixing layer: deterministic models of a turbulent flow. Part 2. The origin of the three-dimensional motion. *J. Fluid Mech.* **139**, 67–95.

FARRELL, B. J. 1989 Optimal excitation of baroclinic waves. *J. Atmos. Sci.* **46**, 1193–1206.

GENT, P. R. & MCWILLIAMS, J. C. 1986 The instability of barotropic circular vortices. *Geophys. Astrophys. Fluid Dyn.* **35**, 209–233.

GILL, A. E. 1982 *Atmosphere-Ocean Dynamics*. Academic. 662 pp.

GREENSPAN, H. P. 1968 *The Theory of Rotating Fluids*. Cambridge University Press. 327 pp.

JOHNSON, J. A. 1963 The stability of shearing motion in a rotating fluid. *J. Fluid Mech.* **17**, 337–352.

KLAASSEN, G. P. & PELTIER, W. R. 1985 The onset of turbulence in finite-amplitude Kelvin–Helmholtz billows. *J. Fluid Mech.* **155**, 1–35.

KLAASSEN, G. P. & PELTIER, W. R. 1989 The role of transverse secondary instabilities in the evolution of free shear layers. *J. Fluid Mech.* **202**, 367–402.

KLAASSEN, G. P. & PELTIER, W. R. 1991 The influence of stratification on secondary instability in free shear layers. *J. Fluid Mech.* **227**, 71–106.

KLOOSTERZEIL, R. C. & VAN HEIJST, G. J. E. 1991 An experimental study of unstable barotropic vortices in a rotating fluid. *J. Fluid Mech.* **223**, 1–24.

LASHERAS, J. C., CHO, J. S. & MAXWORTHY, T. 1986 On the origin and evolution of streamwise vortical structures in a plane, free shear layer. *J. Fluid Mech.* **172**, 231–258.

LASHERAS, J. C. & CHOI, H. 1988 Three-dimensional instability of a plane, free shear layer: an experimental study of the formation and evolution of streamwise vortices. *J. Fluid Mech.* **189**, 53–86.

LESIEUR, M. 1991 *Turbulence in Fluids*. 2nd rev. edn. Dordrecht: Kluwer.

LESIEUR, M., STAQUET, C., LE ROY, P. & COMTE, P. 1988 The mixing layer and its coherence examined from the point of view of two-dimensional turbulence. *J. Fluid Mech.* **192**, 511–534.

LESIEUR, M., YANASE, S. & MÉTAIS, O. 1991 Stabilizing and destabilizing effects of a solid-body rotation on quasi-two-dimensional shear layers. *Phys. Fluids* A **3**, 403–407.

McWilliams, J. C. 1983 On the relevance of two-dimensional turbulence to geophysical fluid motions. *J. Mec. Num. Spec.* 83–98.

McWilliams, J. C. 1984 The emergence of isolated coherent vortices in turbulent flow. *J. Fluid Mech.* **146**, 21–43.

Marcus, P. 1990 Vortex dynamics in a shearing zonal flow. *J. Fluid Mech.* **215**, 393–430.

Melander, M. V., Zabusky, N. J. & McWilliams, J. C. 1988 Symmetric vortex merger in two dimensions: causes and conditions. *J. Fluid Mech.* **195**, 303–340.

Métais, O., Yanase, S., Flores, C., Bartello, P. & Lesieur, M. 1991 Reorganization of coherent vortices in shear layers under the action of solid-body rotation. In *Turbulent Shear Flows*, Munich.

Metcalfe, R. W., Orszag, S. A., Brachet, M. E., Menon, S. & Riley, J. J. 1987 Secondary instability of a temporally-growing mixing layer. *J. Fluid Mech.* **184**, 207–243.

Orszag, S. A. & Patera, A. T. 1983 Secondary instability of wall-bounded shear flows. *J. Fluid Mech.* **128**, 347–385.

Pierrehumbert, R. T. 1986 Universal short-wave instability of two-dimensional eddies in an inviscid fluid. *Phys. Rev. Lett.* **57**, 2157–2159.

Pierrehumbert, R. T. & Widnall, S. E. 1982 The two- and three-dimensional instabilities of a spatially periodic shear layer. *J. Fluid Mech.* **114**, 59–82.

Rayleigh, Lord 1916 On the dynamics of revolving fluids. *Proc. R. Soc. Lond.* A **93**, 148–154.

Shepherd, T. G. 1987 Rossby waves and two-dimensional turbulence in a large-scale zonal jet. *J. Fluid Mech.* **183**, 467–509.

Smyth, W. D. 1992 Spectral transfers in two-dimensional anisotropic flow. *Phys. Fluids* A **4**, 340–349.

Smyth, W. D. & Peltier, W. R. 1989 The transition between Kelvin–Helmholtz and Holmboe instability: an investigation of the overreflection hypothesis. *J. Atmos. Sci.* **46**, 3698–3720.

Smyth, W. D. & Peltier, W. R. 1990 Three-dimensional primary instabilities of a stratified, dissipative, parallel flow. *Geophys. Astrophys. Fluid Dyn.* **52**, 249–261.

Smyth, W. D. & Peltier, W. R. 1991 Instability and transition in finite-amplitude Kelvin–Helmholtz and Holmboe waves. *J. Fluid Mech.* **228**, 387–415.

Smyth, W. D. & Peltier, W. R. 1993 Two-dimensional turbulence in homogeneous and stratified shear layers. *Geophys. Astrophys. Fluid Dyn.* **69**, 1–32.

Waleffe, F. 1990 On the three-dimensional instability of strained vortices. *Phys. Fluids* A **2**, 76–80.

Weiss, J. 1991 The dynamics of enstrophy transfer in two-dimensional hydrodynamics. *Physica* D **48**, 273–294.

Wygnanski, I., Oster, D., Fiedler, H. & Dziomba, B. 1979 On the perseverance of quasi-two-dimensional eddy structures in a turbulent mixing layer. *J. Fluid Mech.* **93**, 325–335.

Yanase, S., Flores, C., Métais, O. & Riley, J. 1993 Rotating free shear flows: Part 1. Linear stability analyses. *Phys. Fluids* A **5**, 2725–2737.